

001
002
003
004
005
006
007
008
009
010
011
012
013
014
015
016
017
018
019
020
021
022
023
024
025
026
027
028
029
030
031
032
033
034
035
036
037
038
039
040
041
042
043
044
045
046

Location-dependent phase transformation kinetics during laser wire deposition additive manufacturing of Ti-6Al-4V

Andrew Huck¹, Amit K. Verma¹, Katie O'Donnell¹, Lonnie Smith¹, Venkata Satya Surya Amaranth Karra¹, Ali Guzel¹, Hangman Chen¹, Petrus C. Pistorius¹, Bryan A. Webler¹ and Anthony D. Rollett^{1*}

¹*Department of Materials Science and Engineering, Carnegie Mellon University, 5000 Forbes Ave, Pittsburgh, 15213, PA, USA.

*Corresponding author(s). E-mail(s): rollett@andrew.cmu.edu;
Contributing authors: ahuck@alumni.cmu.edu;

Abstract

This work models the microstructural evolution as a function of position in laser-wire deposited Ti-6Al-4V parts using a classical multi-component JMAK nucleation and growth model with additive isothermal time steps. Model predictions are compared to experimental observations. The model can be used to interpret nucleation and growth kinetics of various characteristic features of the microstructure that are inaccessible by experiments. It explains the presence of “layer bands” at specific locations unrelated to the weld bead structure. The last re-heating (of multiple thermal cycles) of a solidified layer, and where it peaks, plays a key role in increasing the nucleation density at specific locations, resulting in full α -colony microstructures constituting the “layer bands”, while the rest of the build is predominantly basketweave. Additionally, changes in the basketweave α -lath thickness as a function of the distance from the substrate is studied and compared with an Arrhenius-type function, with results highlighting a more complex relationship than an Arrhenius-type function would suggest.

1 Introduction

Additive manufacturing (AM) is a growing field because it allows rapid prototyping, custom part fabrication, reduced material use, and in situ fabrication of many different designs [1]. Titanium alloys are of prime interest in industries such as aerospace and in the biomedical field because they provide an excellent combination of strength-to-weight ratios and corrosion resistance for service in many demanding applications, while remaining relatively affordable.

Ti-6Al-4V is the most widely used titanium alloy, with an α - β dual microstructure of mostly hexagonal close packed (HCP) α and a small fraction of body centered cubic (BCC) β at room temperature. Extensive research has been performed on AM Ti-6Al-4V to understand the microstructures produced and reduce the uncertainty in its mechanical properties. Within the wide range of AM techniques, welding-scale techniques are of particular interest because of their ability to produce large structures, with significant recent research [2–18]. Laser wire deposition (LWD) is one such technique where feeding a hot wire onto a substrate and simultaneously heating it with a laser creates a molten metal pool and forms a weld bead. Stacking beads layer-by-layer results in a 3-dimensional (3D) part.

AM microstructures vary significantly as a result of the thermal cycling induced by building a 3D part of multiple layers. Microstructures of interest and associated cooling rates for Ti-6Al-4V are well described in Ahmed and Rack [19]. For the studied LWD process, relevant diffusional phases include an allotriomorphic grain boundary α phase (α_{GB}), a Widmanst  tten

sideplate morphology often called colony alpha (α_C), and an intragranular Widmanstätten morphology termed “basketweave” (α_{BW}). At higher cooling rates, above 20 K/s, diffusionless massive (α_m) or martensitic alpha (α') may form, but these microstructures are rarely observed in this process. Consistent with this observation, a recent report has suggested that the minimum cooling rate for martensite formation is (>1000 K/s) [20]. Microstructural features of interest termed “layer bands” are often seen in AM builds similar to the LWD builds of this study [2, 3, 5, 6, 12–16, 18]. There are typically large α_{BW} fractions seen between each of these layer bands and the bands themselves are almost fully α_C (henceforth referred to as (α_{C-LB})).

Previous modeling efforts on the microstructure of Ti-6Al-4V have mostly focused on build-scale feature predictions with limited examination of finer features. Microstructural models for welding scale Ti-6Al-4V AM have used a Johnson-Mehl-Avrami-Kolmogorov (JMAK) [21–25] methodology. To accommodate changing temperatures a “state variable” approach was commonly used, as outlined by Grong [26] and Grong and Shercliff [27]. This approach assumes that the transformation occurs as a sequence of isothermal timesteps and is only dependent on the previous extent transformed and the temperature through a temperature-dependent kinetic function. Morphology extent changes during each time step are assumed to be additive as outlined by Cahn [28] or Christian [29], with the ending point for one step defining the starting point for the next. Kelly [4] was the first to attempt this approach on builds from the Lasform process [30] using kinetic functions sourced from JMatPRO [31] for two morphologies, a combined α_{GB} and α_C morphology and an intragranular α_{BW} morphology. These kinetic functions ($k(T)$) were then used in a JMAK equation to describe the transformation, as in Equation 1.

139

140
141
142

$$\zeta = \frac{V_\alpha}{V} = 1 - e^{-k(T)t^n} \quad (1)$$

143
144
145
146
147
148
149
150
151
152
153
154
155
156
157
158

This approach was also used for gas tungsten arc welding by Charles Murgau [5, 6] and for the LENS process by Irwin et al. [17], adopting the kinetic functions from Kelly. Both approaches again used only a α_{BW} and a combined α_C/α_{GB} morphology. Charles Murgau also modeled evolution of α lath thicknesses ($t_{\alpha-lath}$) and added a model for α' evolution (with α' and α_m considered as the same morphology). Subsequently, both model additions were adopted by Irwin. Makiewicz [11] separated the α_C and α_{GB} morphologies and adopted Kelly's [4] suggested approach to build custom kinetic functions for each morphology using nucleation and growth equations. The general form of the JMAK equation for each morphology was retained.

159
160
161
162
163
164
165
166
167
168
169
170
171
172
173

While significant progress has been made in microstructural predictions on a build scale, work to date has not fully reproduced the layered microstructure observed in Ti-6Al-4V. Additionally, few comparisons have been made of the predictions from the JMAK methodologies used and the actual builds on the scale of hundreds of micrometers. In this work, we employ the JMAK approaches outlined above with close examination of the inputs to predict the microstructure constituents as a function of position in a LWD Ti-6Al-4V bead. A comparison between experimental data and modeling results is presented on a more granular scale ($= 100 \mu m$) compared to other work.

174
175176

2 Experimental Methods

177
178179

2.1 Materials and Fabrication Methods

180
181
182
183
184

Ti64 samples were manufactured using a LWD system (Wolf Robotics LmWD). Deposition was performed using 1.5875 mm diameter Ti-6Al-4V welding wire

(per AMS 4954K specification), using a Ti-6Al-4V substrate (per AMS 4911R specification). The build configuration was a stacked wall bead-on-bead structure, built with each bead deposition starting at the same end and deposited vertically from the plate in the z-orientation. Beads were deposited for a minimum length of 200 mm to reach a steady state in a controlled inert argon purged environment, preventing the formation of an α -case. Build parameters were as follows for the specific build studied in this work: Laser power of 3000 W, wire power of 150 W, robot travel speed of 2 mm/s and wire feed rate of 25.8 mm/s.

2.2 Sample Preparation and Microscopy

All samples were cut and sectioned from the steady state deposition regions to fit a 31.75 mm diameter mount using electrical discharge machining (EDM). Stacked beads with heights exceeding the mount diameter were further sectioned to fit multiple mounts. Samples were mounted in Buehler KonductoMet phenolic powder, and polished for metallographic analysis using the following three step procedure adapted from VanderVoort [32].

1. Wet grind with 320 grit SiC paper until samples are co-planar (6 lbs of force per sample, 240 rpm base speed, 50 rpm head speed, complementary rotation).
2. Rough polish with 9 μm diamond suspension and Buehler MetaDi Lubricant for 10 min on a Buehler Ultra-Pad (6 lbs of force per sample, 120 rpm base speed, 50 rpm head speed, opposite rotation).
3. Final polish with a mixture of 70% colloidal silica and 30 % hydrogen peroxide (3 % concentration) for 10 min on a Leco Imperial Microcloth (6 lbs of force per sample, 120 rpm base speed, 50 rpm head speed, opposite rotation). Wet polish with water for 2 min to clean samples.

6 LWD Phase Transformations in Ti64

231 Sample polishing was performed on a Buehler EcoMet 250, and samples were
232 cleaned using DI water in an ultrasonic cleaner for 10 min following each
233 preparation step. Following polishing, samples were etched by submerging in
234 Kroll's Reagent for a minimum of 15 sec. Samples were observed optically, then
235 step 3 was repeated to re-polish the samples for scanning electron microscopy
236 (SEM).

237
238
239
240 Bead quality for both single and stacked beads was assessed visually and
241 assigned a score ranging from one to four: 1 representing an intermittent bead
242 (i.e., dripping), 2 a variable bead, 3 a rippled bead, and 4 a smooth bead.
243 Samples with a score of 1 were not assessed any further because of their poor
244 potential for builds. Single and stacked bead widths were also measured at
245 their widest point using a pair of electronic calipers. The height of deposition
246 was also measured for stacked wall beads using electronic calipers.

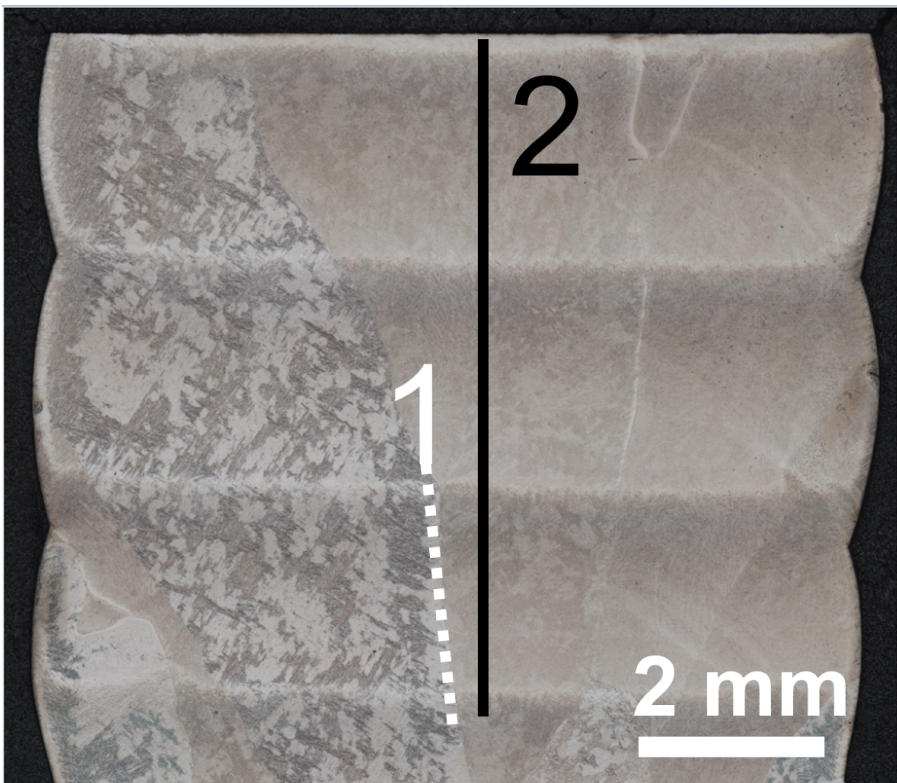
247
248 Optical microscopy (OM) was performed using using a Zeiss LSM 800 Con-
249 focal Microscope. Tile images were taken at 500x for each sample and stitched
250 together to create one mosaic image for each sample. For both single bead and
251 stacked wall beads the fusion zone area, fusion zone width, fusion zone depth,
252 bead widths, and heat affected zone depth were measured. For stacked wall
253 beads the height of the transient region, height of the characteristic region,
254 number of layer bands, spacing between layer bands, vertical position of each
255 band above the substrate, and the areas of the transient and characteristic
256 region were measured ([Figure 5](#)). Prior beta grain sizes were also measured
257 for both single and stacked wall beads, parallel and perpendicular to the build
258 direction using the Heyn lineal intercept procedure outlined in ASTM E112-12
259 [\[33\]](#). All optical microscopy measurements were taken using ImageJ [\[34\]](#). SEM
260 was also performed on samples after repolishing using a Tescan Mira 3 field
261 emission gun (FEG) instrument at 10 kV accelerating voltage.

2.3 Quantification of Microstructural Features 277

On a 15-bead stacked build, a series of images were taken along a prior β grain boundary (Line 1 in [Figure 1](#)) for estimation of α_{GB} , α_C , and α_{BW} volume fractions. The thickness of the α_{GB} morphology and the distance the α_C morphology grew from the α_{GB} were measured through the series of images, with the assumption that this represents the general trend through the rest of the characteristic layers and across grain boundaries. The number of prior β grain boundaries were then counted to obtain an average across the height of the characteristic layer. Multiplication of the α_{GB} thickness and α_C growth distance by the number of prior β grain boundaries then yielded a total assumed distance in the horizontal slice of the build for each morphology, with the rest assumed as α_{BW} . Division by the average width of the build across the characteristic layer yielded a morphology fraction for the height of the representative image.

Another series of images was taken in the middle of a prior β grain (Line 2 in [Figure 1](#)) to characterize the microstructural features in detail, focusing on α lath thicknesses and microstructural morphologies in the center of the prior β grains. A computer vision method was used to measure the thickness of the laths in each image [35] through the height of the line, with the trend observed assumed to be representative of that in similar regions of the build. Images were also taken at approximately 500 μm spacing through the rest of the height of the build to establish a larger trend of lath thicknesses. Line 2 was also used to gauge trends in α morphology in the center of the grain. A rule was applied that if packet size, i.e., a series of parallel laths, was less than 10, then the microstructure in the image was classified α_{BW} . Combined with the information in Line 1, defining a packet size allowed estimation of α_C and α_{BW} fractions as a function of (vertical) height.

323
324
325
326
327
328
329
330
331
332
333
334
335
336
337
338
339
340
341
342
343
344
345
346
347



348 **Fig. 1** Optical image of a portion of stacked 15-bead build, (shown in full in [Figure 5](#)),
349 highlighting characteristic prior β grains and other features. White horizontal lines at regular
350 intervals, colloquially termed “layer bands”, can be observed along with cycles of gradual
351 darkening moving up between layer bands. To quantify components of the microstructure,
352 a series of images at 5000x were taken: the first along the prior β grain boundary (labeled 1)
353 and the second at the center traversing three layer bands and the area in between (labeled 2).

353

354

3 Microstructure Model

355

356

357

3.1 Model Setup and Purpose

358

359

360

361

362

363

364

365

366

367

368

A microstructural model was built and calibrated in Python 3.7/3.8 [36] based on the material characterization results from this study to model the β to α phase transformation. The purpose of this model was to provide pre-build insight into the microstructures resulting from different thermal histories and to understand microstructural changes on a finer scale. The desired specific

predictions at a given location were the fractions of α_{GB} , α_C , α_{BW} , and α' in the final microstructure as well as the α_{BW} lath thicknesses formed.

3.2 Thermal Histories for this Study

The thermal history is a critical input for predicting location-dependent transformation behavior. The current model can accept any thermal history input. For the calculations reported in this paper, the evolution of the temperature profile in builds was calculated using a one-dimensional layer model, using an explicit enthalpy-based finite-difference approach. A one-dimensional model is a reasonable approximation, given the horizontal orientation of the characteristic microstructural bands (indicating that the lateral temperature differences are small) and that the test builds are long (in the laser travel direction) compared with the thickness of the deposit. In the model calculations, a defined volume of material (based on layer thickness and deposit width) was added to the build at set time intervals, and a certain increment of heat transferred to the top of the build. The additional energy was added at a constant rate to the deposited volume over a defined time period (taken to be equal to the laser spot size of 7.6 mm divided by the laser speed). Laser absorptivity was varied to match the observed layer-band positions, with a typical value around 0.4[37].

Boundary conditions were as follows: Convective and radiative heat transfer occurred from the sides and top of the deposit, using an emissivity of 0.4, and a convective heat transfer coefficient of $10 \text{ W/m}^2\text{K}$. Conduction to the base was approximated using a constant base temperature and pseudo-steady-state conduction, using the shape factor for conduction between parallel rectangular surfaces[38]. Temperature-dependent material properties (enthalpy and density – used to calculate volumetric enthalpy and thermal conductivity) were

415 taken from the compilation of Mills[39]. The thermal conductivity of the liquid
 416 was increased by a factor of 15 to approximate the effect of convection.
 417

418

419 3.3 Microstructure Model Physical Description

420

421 This model uses a JMAK equation in the form of [Equation 1](#), with the kinetic
 422 function and time broken down into nucleation and growth terms. This forms
 423 an “extended volume” as shown in [Equation 2](#), which is then corrected for
 424 impingement by the overall JMAK equation. Nuclei are assumed to form
 425 spherically with parabolic growth.
 426

427

428

$$429 \quad V_e = k(T)t^n = \frac{4\pi}{3} \int_0^t I_0 r^3 dt \quad (2)$$

430

431 A schematic flow chart of the model for a single time-step, considered
 432 isothermal with the temperature derived from the thermal history, is presented
 433 in [Figure 2](#). For each time-step, the amount of α at equilibrium for the cor-
 434 responding temperature (α_{eq}) is calculated and compared with the amount of
 435 α from the previous time-step. If the amount of prior α exceeds α_{eq} , disso-
 436 lution occurs, otherwise α is allowed to grow from the remaining β fraction.
 437 Four alpha morphologies are considered for the β to α phase transformation.
 438 Diffusional phases modeled are α_{GB} , α_C , and α_{BW} , with α' martensite also
 439 considered as a diffusionless phase. These morphologies are allowed to grow
 440 simultaneously. Subsequently, correction is made for the impingement of multi-
 441 ple growing phases, leading to corrected fractions for the time-step. The process
 442 is then repeated for the next time-step at the corresponding new temperature.
 443

444

445

446

447

448

449

450

451

452

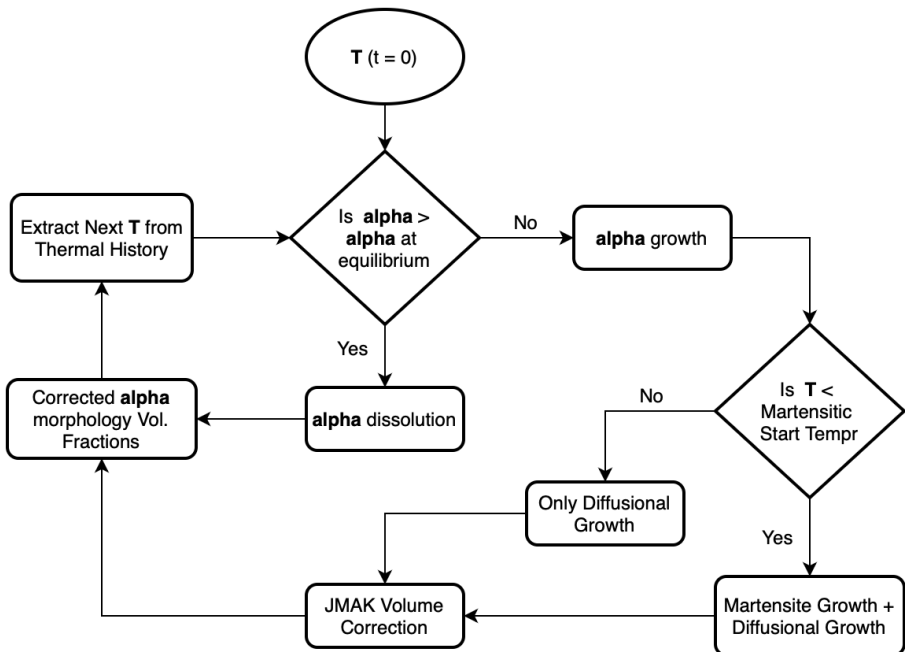


Fig. 2 Schematic process flow of the model, highlighting the iterative nature of calculations as temperature changes in each time-step, with α morphology fractions the primary outputs. T stands for temperature, t for time and JMAK for Johnson-Mehl-Avrami-Kolmogorov methodology.

To obtain a final predicted microstructure for many locations in the build, this process is applied for the thermal history at each location. The final extent of each morphology and the final predicted lath thickness can then be plotted in cross-section.

3.3.1 Governing Transformation Equations

The heterogeneous nucleation model has the form shown in [Equation 3](#). The details of the heterogeneous nucleation model are given in [Appendix A.1](#).

$$I_0 = \frac{dN}{dt} = N_0 e^{-Q/kT} \quad (3)$$

12 *LWD Phase Transformations in Ti64*

507 Growth is modeled using a Zener approximation, as shown in [Equation 4](#),
 508 with vanadium assumed to be the slow diffuser in the β phase. Additional
 509 details are provided in Appendix A.2.
 510

511

$$512 \quad r = \int_0^t \nu dt = \frac{X_{V_0} - X_{V_\beta}}{(X_{V_\alpha} - X_{V_\beta})} \sqrt{D_V t} \quad (4)$$

513

514 The diffusionless martensitic transformation is modeled using a Koistenin-
 515 Marburger equation [\[40\]](#), as shown in [Equation 5](#).
 516

517

$$518 \quad \zeta' = X_\beta [1 - e^{-C_{MB}(T_{MS} - T)}] \quad (5)$$

519

520 Thermodynamic values are sourced from the Thermo-Calc TCTI2
 521 database[\[41\]](#).
 522

523

524 **3.3.2 Corrections for Multiple Growing Morphologies and** 525 **Incomplete Transformation**

526

527 The JMAK equation in the form of [Equation 1](#) and [Equation 2](#) models a sin-
 528 gle growing phase, random nucleation events, a complete transformation, and
 529 spherical growth [\[29\]](#). The correction for impingement occurs by [Equation 6](#),
 530 with dV^α and dV_e^α representing the real and extended volumes of transformed
 531 α and $\frac{V^\alpha}{V}$ representing the extent transformed by dividing the volume trans-
 532 formed (V^α) by the total system volume (V). Integration of this expression
 533 leads to [Equation 1](#), as described by Christian [\[29\]](#).
 534

535

$$536 \quad dV_\alpha = dV_\alpha^e \left(1 - \frac{V^\alpha}{V} \right) = dV_\alpha^e (1 - \zeta) \quad (6)$$

537

538 When multiple phases or morphologies are growing a correction must be
 539 made to make [Equation 6](#), as outlined by Jones and Bhadeshia [\[42\]](#). Taking
 540 their approach and adapting it for an incomplete transformation, [Equation 6](#)
 541 was transformed to [Equation 7](#), with the i subscript denoting one particular
 542

phase or morphology and the summation denoting all phases or morphologies growing simultaneously. 553
554
555
556

$$dV_i = dV_i^e \left(1 - \frac{\sum V_i}{V_{eq-\alpha}} \right) = dV_i^e (1 - \zeta_i) \quad (7)$$

The second correction to be made accounts for the incomplete nature of the transformation, with the final state in a two-phase field by the reaction $\beta \rightarrow \alpha + \beta'$, with β' being a phase enriched in vanadium and deficient in aluminum. This is solved by modifying the extent as follows in [Equation 8](#), where $V_{eq-\alpha}$ is the equilibrium amount of the α phase possible as a function of temperature. 557
558
559
560
561
562
563
564
565
566
567
568
569
570
571
572
573
574

$$\zeta = \frac{V_\alpha}{V_{eq-\alpha}} \quad (8)$$

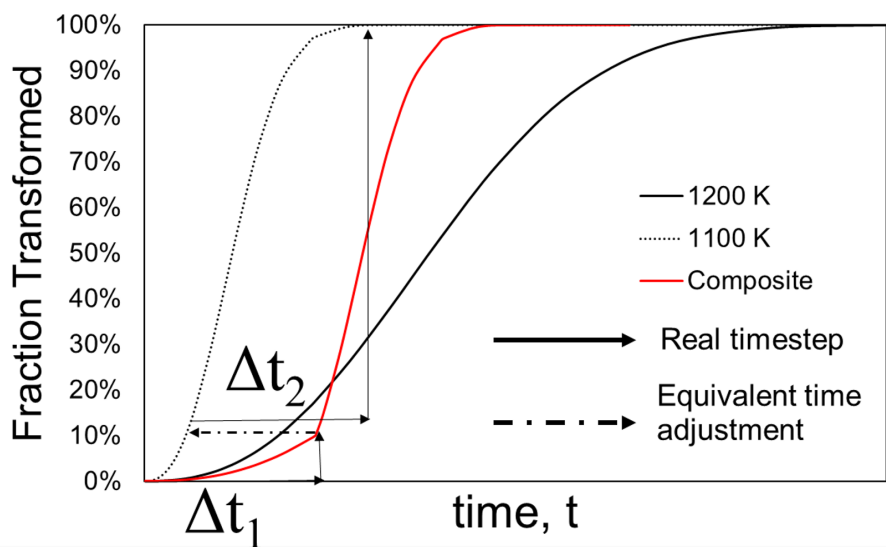
3.3.3 α Equilibrium and Dissolution

The extent of α at equilibrium was determined from Thermo-Calc as described in Appendix B.4. For α dissolution, Kelly [4] proposed a model for movement of the $\alpha - \beta$ interface with parabolic growth during heating of Ti64 after Whelan [43]. Given the moderately fast transformation to β and low dissolution lag from Kelly's model, dissolution for this study is modeled by assigning the total α fraction as equivalent to α_{eq} upon heating with no lag. Dissolution is considered hierarchically, with the last phase to form dissolving first. This assumes the last formed interfaces have the highest energies. Thus, dissolution occurs in the order: α' , α_{BW} , α_C , α_{GB} . 575
576
577
578
579
580
581
582
583
584
585
586
587
588
589
590

3.3.4 Considerations for Additivity

Critical to the additive approach used here in a JMAK formulation is using a concept referred to by Kelly [3] as "equivalent time" and by Charles-Murgau [5] as "fictive time". Any TTT diagram shows that the start and end times 591
592
593
594
595
596
597
598

599 for transformation are a function of temperature, as expected. This also
 600 implies that there are different physical times that correspond to the same sig-
 601 moidal transformation extent at different temperatures. Thus, it is necessary
 602 as temperature changes to ascertain what “equivalent time” at the current
 603 temperature corresponds to the transformation extent from the previous time
 604 step when forecasting the change in extent for the next time step. This can be
 605 seen schematically in [Figure 3](#).
 610
 611



629 **Fig. 3** Diagram showing the shift in the equivalent time required at the beginning of each
 630 time step to identify the correct transformation extent on the curve at the new temperature.
 631 Solid curve shows transformation curve for first temperature and time, Δt_1 . A shift is then
 632 performed to find the equivalent time on the curve at the new temperature for the next time
 633 step so that another time step, Δt_2 can be taken. The combined curve shows the simulated
 634 transformation.
 637
 638

639 Mathematically, this proceeds as follows: assuming a constant nucleation
 640 rate and a parabolic growth rate, [Equation 2](#) integrates to the form of
 641

Equation 9, with an Avrami exponent (n) of $\frac{5}{2}$, a combination of 1 from nucleation and $\frac{3}{2}$ for growth. 645
646
647
648

$$V_e = \frac{8\pi}{15} I_0 \nu^3 t^{5/2} \quad (9) \quad 649
650
651$$

This can then easily be solved for time, which can be seen in Equation 10. 652
653
654

$$t_{equivalent} = \left(\frac{15V_e}{8\pi I_0 \nu^3} \right)^{2/5} \quad (10) \quad 655
656$$

To obtain a value for V_e to plug into this equation, the extent calculated from the previous time step is used. This extent must be converted to an extended volume using Equation 11. 657
658
659
660
661
662
663

$$V_e = -\ln(1 - \zeta_{old}) \quad (11) \quad 664
665$$

Combining Equation 9 and Equation 10 allows for calculation of the time it would take to reach the current transformation extent at the new step temperature. Finally, the change in time for the current time step is applied (Δt_2) to find the transformation extent after that time step using the correct forms of Equation 1 and Equation 2, as shown in Figure 3. This process is scalable to as many time and temperature steps as are available to minimize temperature differences between steps. 666
667
668
669
670
671
672
673
674
675
676
677
678
679
680

3.3.5 JMAK Model Parameters

Different assumptions in Equation 2 led to different forms of Equation 1 and Equation 2 for this study. This was particularly relevant in examining nucleation of the α_{GB} and α_C morphologies. Kelly [4], Charles [5, 6], Irwin [17], and Makiewicz [11] all used an Avrami exponent (n in Equation 2) of $\frac{5}{2}$ for all diffusional phases, implying constant nucleation and parabolic growth with spherical geometry. Constant nucleation is reasonable for the intragranular 681
682
683
684
685
686
687
688
689
690

16 *LWD Phase Transformations in Ti64*

691 α_{BW} morphology and is adopted for this study, with an Avrami exponent con-
692 tribution of 1. Although α_{BW} likely nucleates at specific sites, nucleation could
693 be envisioned as random with only some sites activated in any time interval
694 if sites are distributed mostly randomly. However, constant nucleation for the
695 α_C phase seems incorrect, particularly in context of the work of Fujii [44] and
696 later Sun et al. [45] in Ti-6Al-2Zr-1Mo-1V (TA15). TEM images taken by Fujii
697 suggest that $\alpha_{GB} - \beta$ interfacial perturbation is the mechanism that initiates
698 colony growth rather than strict nucleation. Pragmatically, modeling this as
699 nucleation can be justified because there is little difference between a pertur-
700 bation and nucleation site formed along the interface, assuming little to no
701 “nucleation barrier” is applied or under the assumption that the nucleation
702 barrier for the initiating α_{GB} morphology must still apply. Modeling with con-
703 stant nucleation does not seem appropriate for α_C because initiation can only
704 happen at certain sites and the growing parallel lamellae of the colony should
705 pinch out any subsequently nucleated lamellae. This means all sites of plausi-
706 ble growth should be saturated very quickly and subsequent nucleation events
707 are unlikely, leading to an assumption of all nucleation occurring at time zero
708 for α_C and a JMAK exponent contribution of 0. This has also been applied
709 for the α_{GB} morphology, as formation is only possible in the limited area of
710 prior β grain boundaries. Nucleation of α_{GB} should occur rapidly (given the
711 low nucleation barrier) and then cease. Growth for all diffusional morpholo-
712 gies is assumed to be parabolic, leading to a JMAK exponent contribution of
713 $\frac{3}{2}$. This leads to total JMAK exponents (**n**) of $\frac{3}{2}$ for α_C and α_{GB} and $\frac{5}{2}$ for
714 α_{BW} . A summary of parameters used is tabulated in [Table I](#).

730
731
732
733
734
735
736

Table I Summary of parameters used in JMAK functions

Parameter	Units	α_{GB}	α_C	α_{C-LB}	α_{BW}	
N_0	sites/(m ³ * s)	$5 \cdot 10^{16}$	$2 \cdot 10^{17}$	$4 \cdot 10^{19}$	$3 \cdot 10^{20}$	737
$\theta_{\alpha-\beta}$	Degrees	5	5	5	5	738
ΔG_S	J/m ³	0	$0.5 \cdot 10^6$	$0.5 \cdot 10^6$	$45 \cdot 10^6$	739
n		3/2	3/2	3/2	5/2	740
						741
						742

3.3.6 α Lath Thickness Modeling

α lath thicknesses are modeled after the approach of Charles-Murgau [5] according to Equation 12, with t_{lath}^n representing the lath thickness in the previous step and $x_{\alpha_W}^n$ representing the total Widmanstätten fraction present at the previous time. The corresponding deltas (Δ) represent the change in these variables during the current time step.

$$t_{lath}^{n+1} = t_{lath}^n + \Delta t_{lath} = \frac{t_{lath}^n x_{\alpha_W}^n + t_{lath}^{eq} \Delta x_{\alpha_W}}{x_{\alpha_W}^n + \Delta x_{\alpha_W}} \quad (12)$$

This approach assumes that there is an increasing number of nucleation events as temperature decreases, leading to a smaller “equilibrium” lath size formed at that temperature, t_{lath}^{eq} . On this basis, an Arrhenius type equation is used to model the t_{lath}^{eq} parameter, as shown in Equation 13.

$$t_{lath}^{eq} = k_{lath} e^{-Q/RT} \quad (13)$$

The values k and Q/R are used as fitting parameters to match the observed results. A starting lath size (t_0) is necessary in this method for the first calculated α to form (t_{lath}^n in Equation 12). Charles-Murgau [5] outlined two different sets of values from Gil et al. [46] and Irwin et al. [17] for these parameters. This study observed significantly smaller lath thicknesses than those predicted by either set, therefore a different set was introduced for smaller overall thicknesses. The values are tabulated in Table II, with a comparison over the relevant temperature range in Figure 4.

783
784
785
786
787
788
789
790
791
792
793
794
795
796
797
798
799
800
801
802
803
804
805
806
807
808
809
810
811
812
813
814
815
816
817
818
819
820
821
822
823
824
825
826
827
828

Table II Parameters used to estimate Widmanstätten lath sizes

Parameter	Gil	Irwin	This Study
$k \text{ } (\mu\text{m})$	18400	1.42	5
Q/R (K)	10044	294	2300
$t_0(\mu\text{m})$	1	1	0.5

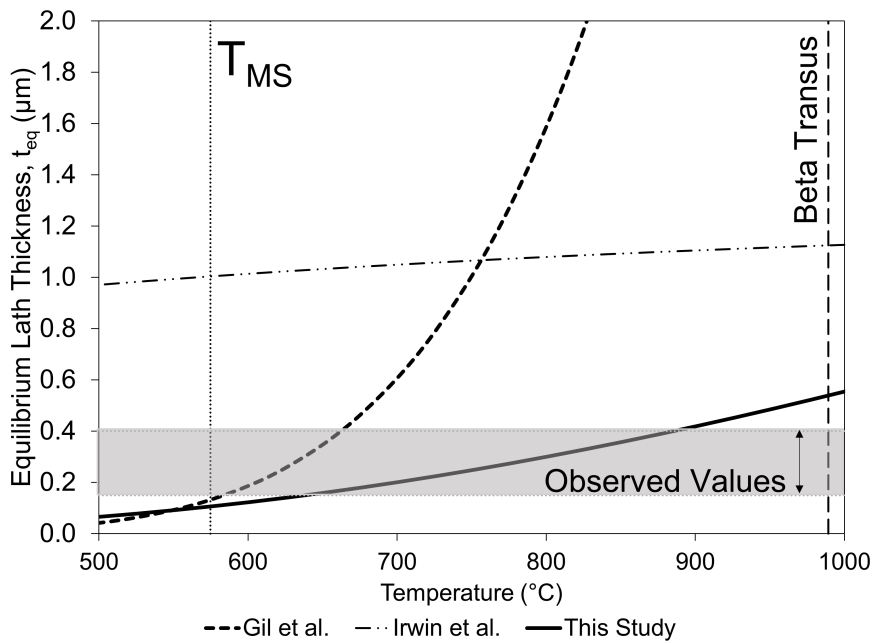


Fig. 4 Calculated equilibrium lath thicknesses over a typical temperature range for diffusional transformation in Ti64 using a variety of different constants, after Charles-Murgau [5].

4 Results

4.1 Microstructural Observations

4.1.1 At Sample Scale

The stacked bead builds printed in this study exhibit varying optical properties highlighting microstructural differences along the build, with an example shown in Figure 5. Broadly, two overall regions are visible, with the bottom “Characteristic” region comprising $\approx 2/3$ of the build, and the lighter

“Transient” region comprising the remainder at the top. While the transient region appears to have relatively consistent optical properties, the characteristic region is composed of many repeating layers, henceforward referred to as “characteristic layers”. These layers exhibit a clear pattern of small lighter features termed “layer bands” followed by gradual darkening, with the cycle then repeating in the next layer. For Figure 5, there are thirteen characteristic layers with thickness varying between 1.9 and 2.6 mm. The thinner and lighter layer bands are on the order of 100-200 μm in thickness. The positions of the characteristic layers depend on the sub-solidus thermal histories and do not align with the positions of the deposited beads of metal.

829
830
831
832
833
834
835
836
837
838
839
840
841
842
843
844
845
846
847
848
849
850
851
852
853
854
855
856
857
858
859
860
861
862
863
864
865
866
867
868
869
870
871
872
873
874

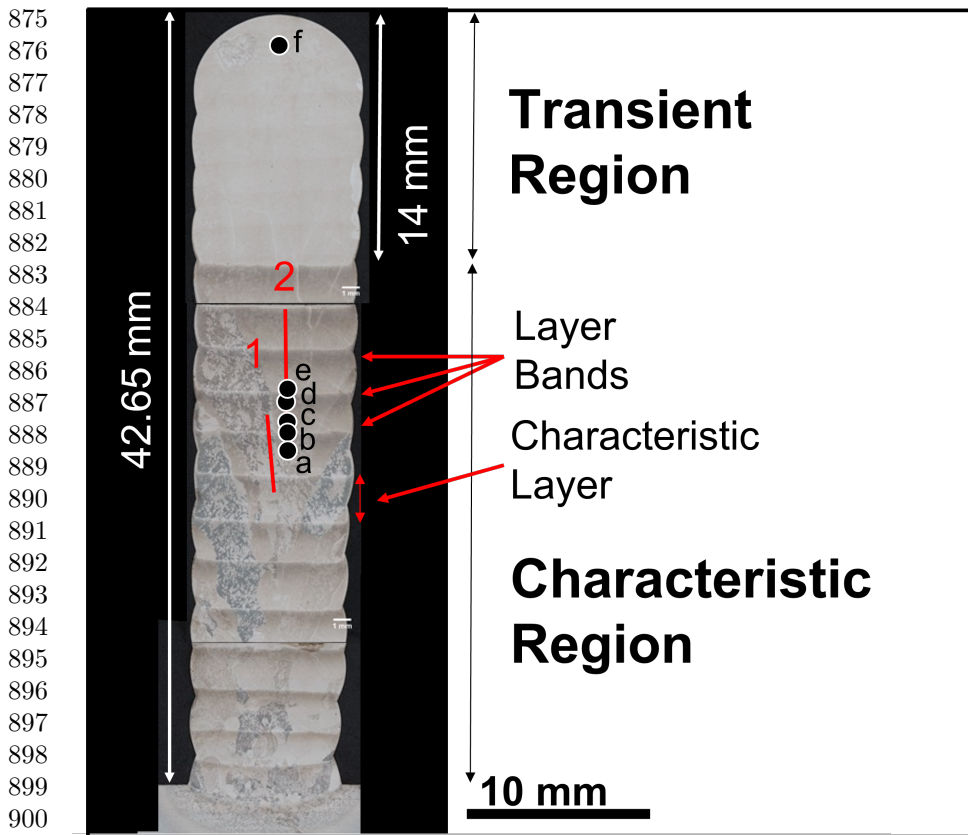


Fig. 5 Cross-Sectional view of stacked fifteen bead build using optical microscopy. Regions termed “Characteristic” (Figure 6) and “Transient” (Figure 8) are clearly distinguishable, as are the features called “layer bands” (Figure 7) dividing each characteristic layer. Also pictured are Lines 1 and 2 from Figure 1, with selected points labeled for future figures.

While the individual beads in Figure 5 are difficult to distinguish, all fifteen beads can be seen from the curvature present on the outside of the cross-section. There are just over four beads in the transient region and just under eleven in the characteristic region. The β microstructure clearly coarsens from bottom to top, with much smaller grain sizes at the baseplate. Large prior β grains are visible starting roughly 10 mm above the baseplate. These grains are similar in size to previous studies [4, 5] with similar processing conditions.

Grains are several millimeters wide in the horizontal direction and are elongated in the vertical stacking direction, commensurate with epitaxial growth under vertical heat flow.	921 922 923 924 925 926 927 928 929 930 931 932 933 934 935 936 937 938 939 940 941 942 943 944 945 946 947 948 949 950 951 952 953 954 955 956 957 958 959 960 961 962 963 964 965 966
4.1.2 At Microstructure Scale	927 928
Scanning Electron Microscope (SEM) images were captured using a TESCAN MIRA-3 FEG in back scatter mode at 10 keV, with a working distance of 8–9 mm and 5000× magnification, obtaining an area of 50 × 50 μm^2 . This magnification provides a reasonable pixel resolution (1024 × 1144 pixels) and a sufficient number of features to count for comparison across the builds. Observed microstructures most closely resemble those of the annealed AM builds reported by Liu et al. [1] as well as those of previous similar scale DED studies [2, 5, 12, 17]. The scale of the deposited beads resulted in cooling rates that were significantly lower than the Laser Powder Bed Fusion or Selective Laser Melting builds referenced by Liu et al., with little α' observed. α_{BW} was the dominant phase observed throughout the height of stacked builds, with some typical examples from the characteristic region shown in Figure 6.	929 930 931 932 933 934 935 936 937 938 939 940 941 942 943 944 945 946 947 948 949 950 951 952 953 954 955 956 957 958 959 960 961 962 963 964 965 966

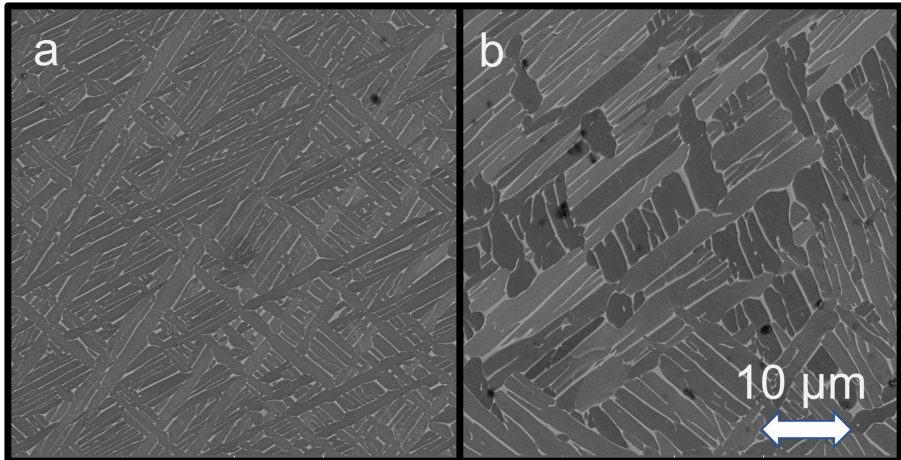


Fig. 6 BSE SEM Image of characteristic region α_{BW} taken at 15 keV. a) is point c in Figure 5, at the bottom of a characteristic layer while b) is point d at the top of the same layer. The difference between the two images demonstrates the coarsening that occurs with increasing height in each characteristic layer.

α_{GB} was present on the prior β grain boundaries, but was small in scale given the multi-millimeter wide prior β grains. Minor α_C growing from the α_{GB} phase was observed, but lengths were generally limited to tens of μm , limiting the total fraction of this morphology as a result of the rapidly coarsening prior β grains.

The characteristic region had some significant differences in line with optical observations, most notably the light “layer band” features observed. These features have been reported by a number of previous researchers from similar scale direct energy deposition builds [3, 5, 15, 17, 18]. While the bulk of the build exhibited a microstructure dominated by α_{BW} , the fine layer bands were nearly entirely comprised of α_C , although of a slightly different nature than the primary α_C growing from the α_{GB} morphology. Colony sizes, defined as the number of parallel lamella, were smaller than in the primary α_C , did not

appear to exclusively grow from the α_{GB} phase and were similar in character to the “packet colony” described by Kelly [3]. An example can be seen in Figure 7.

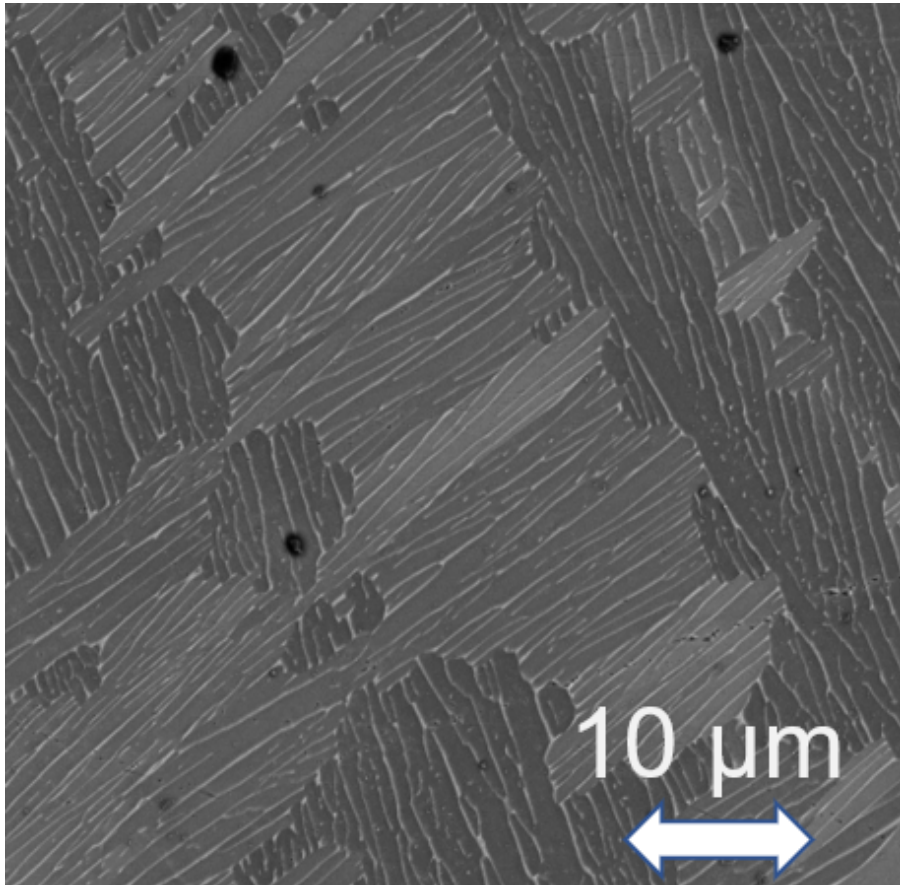
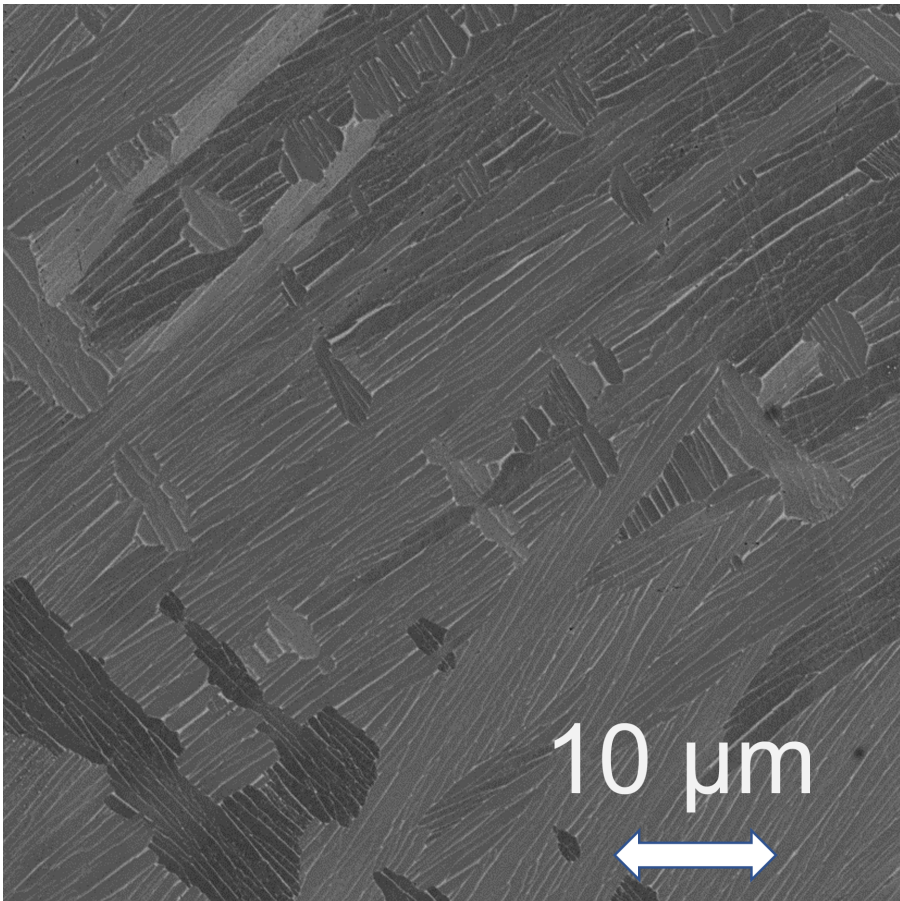


Fig. 7 SEM Image of characteristic region layer band (point b of Figure 5), the light features in the characteristic region of Figure 5. Note the parallel α_C packets that are intermingled instead of assuming mostly one orientation from a prior β grain boundary

The transient region contained numerous features that resembled low number (<10) α_C packets intermixed with α_{BW} , which was unexpected given the rather uniform optical appearance. An example is shown in Figure 8. This phenomenon was also reported in the top of LWD builds by Baufeld et al. [15]

1059 and is still an anomaly. These microstructures are similar to those seen in the
1060 characteristic region detailed above, but appear distinct enough to be treated
1061 as a separate microstructure type in this context.
1062
1063
1064



1093
1094 **Fig. 8** SEM Image near top of transient region (point f in [Figure 5](#)) showing the apparent
1095 packet α_C like appearance of much of that region, with α_{BW} intermingled in other areas
1096
1097

1098 Lath sizes varied across each characteristic layer in a repeating pattern (0.4-
1099 0.7 μm), with some additional variability within the transient region (0.3-0.4
1100 μm). Results are compared to predicted values in the next section.
1101
1102
1103
1104

4.2 Microstructural Modeling Results

C-curves generated for diffusional α morphologies can be seen in Figure 9 along with curves used by Kelly [4] from kinetic functions for comparison. The generated curves were optimized by changing the input parameters for the nucleation and growth functions to fit the observed results in the stacked build shown in Figure 5.

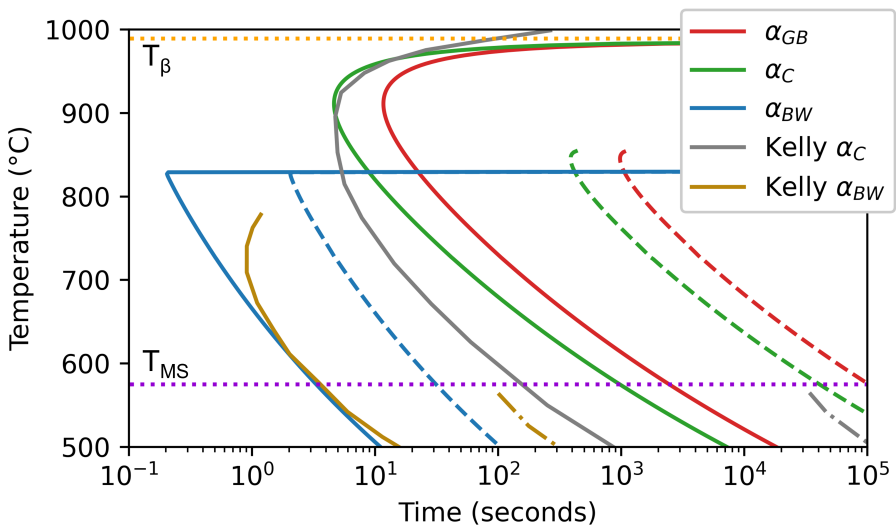


Fig. 9 Transformation curves for 1 % (solid) and 95 % (dashed) of the α_{eq} value for the listed α morphologies (Note: % values are the fraction of equilibrium α rather than total). Also shown are the curves used by Kelly [2, 3] derived from Thermo-Calc. The calculated β transus temperature is shown as a dotted line labeled T_β and the Martensite start temperature is dotted and labeled as T_{MS} .

An additional C-curve for the accelerated α_{C-LB} morphology is shown in Figure 10. This curve was obtained by increasing the nucleation site density for α_C significantly in Equation 3, as shown in Table I. This promotes sufficient α_C formation to correspond with observed layer band morphology fractions before the temperature falls enough to provide sufficient driving force for α_{BW}

1105
1106
1107
1108
1109
1110
1111
1112
1113
1114
1115
1116
1117
1118
1119
1120
1121
1122
1123
1124
1125
1126
1127
1128
1129
1130
1131
1132
1133
1134
1135
1136
1137
1138
1139
1140
1141
1142
1143
1144
1145
1146
1147
1148
1149
1150

nucleation at the observed cooling rates. The increased nucleation sites are presumed to be undissolved alpha that remains when the material is heated to the vicinity of the beta transus[18]. As discussed below, the increased nucleation site density was necessary to match (approximately) the observed prevalence of colony alpha in the light-etching bands.

1159

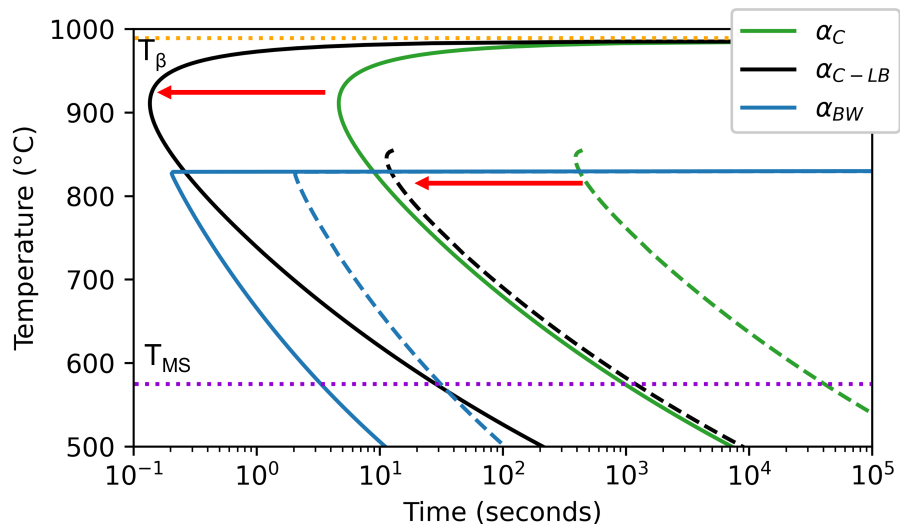


Fig. 10 Schematic transformation curves for α_C and accelerated α_{C-LB} layer band colony morphology, as well as α_{BW} for comparison. Red arrows denote effect of simply changing N_0 in [Equation 3](#), accelerating the growth of α_C so that the nose is now above the curve for α_{BW}

1182

1183

A single point output of the microstructure model from a simulated thermal history is shown in [Figure 11](#), corresponding to point *a* in [Figure 5](#), with eight temperature peaks visible representing eight thermal cycles. The top panel shows temperature as a function of time, calculated with the one-dimensional model, with the β transus temperature (T_β) as a black dashed line. The middle panel shows the evolution of α phase morphologies volume fractions, with the remainder β phase, while the bottom panel shows the evolution of lath thickness (T_{lath}) through the build process, as predicted by [Equation 10](#).

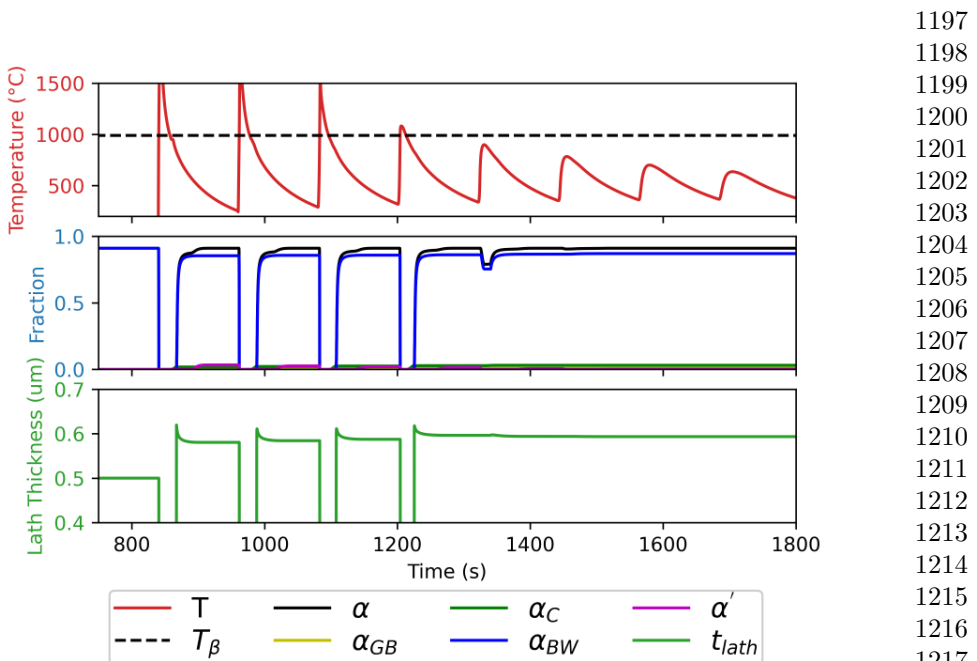
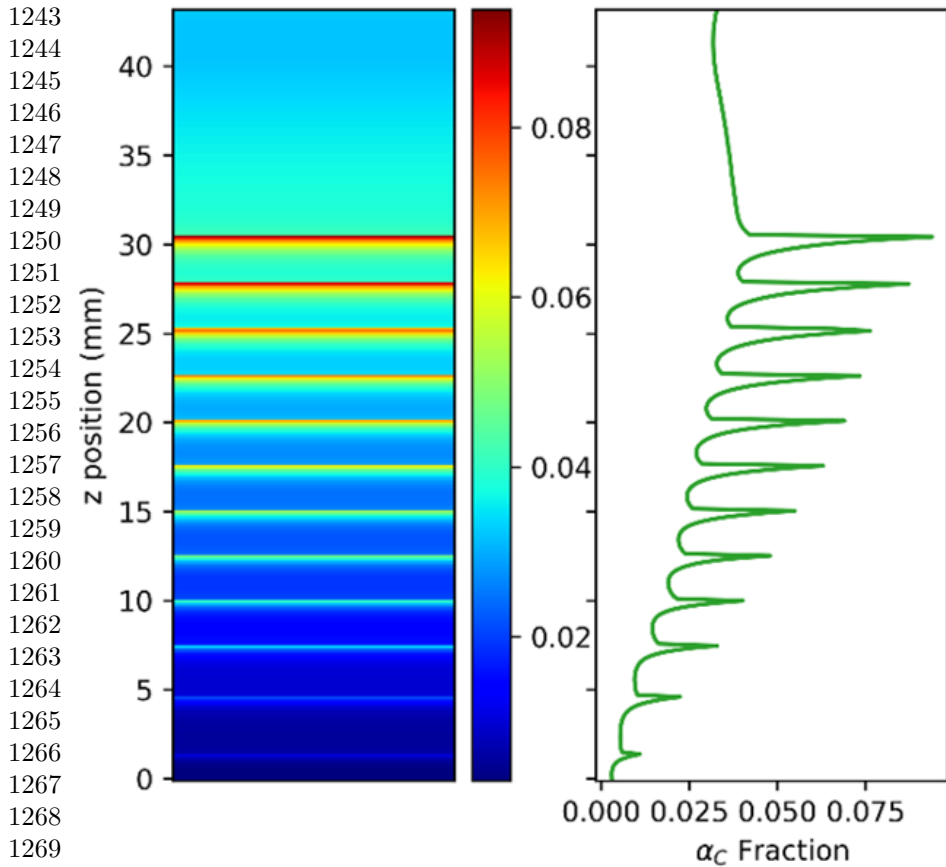


Fig. 11 Single-point run of microstructure model showing the forecasted evolution in α morphology and lath thickness for the shown thermal history. The point simulated is point *a* in Figure 5. Deposition began just after 800 seconds, thus the earlier times are not shown.

A 1D heat map of the α_C morphology was obtained (Figure 12 left) using the same thermal results. The right panel in Figure 12 shows the corresponding value of α_C for easy visualization. While α_C peaks correspond closely to layer band locations in Figure 5, the volume fraction of α_C is not nearly as high as those observed. To correct this, the nucleation site density for α_C was increased (Table I / Figure 10) when the peak temperature at a given location was less than 10 K below the β transus. Results with this change are plotted in Figure 13, demonstrating an increase in the magnitude of the α_C peaks in accordance with the observed layer bands.

1197
1198
1199
1200
1201
1202
1203
1204
1205
1206
1207
1208
1209
1210
1211
1212
1213
1214
1215
1216
1217
1218
1219
1220
1221
1222
1223
1224
1225
1226
1227
1228
1229
1230
1231
1232
1233
1234
1235
1236
1237
1238
1239
1240
1241
1242



1271 **Fig. 12** 1D vertical output of microstructural model to simulate the stack seen in [Figure 5](#).
1272 At the left is a heat map of the α_C morphology with height, with the right panel showing
1273 the corresponding values of α_C . The left panel by design replicates the general appearance
1274 of [Figure 5](#) in banding.
1275

1276
1277
1278
1279
1280
1281
1282
1283
1284
1285
1286
1287
1288

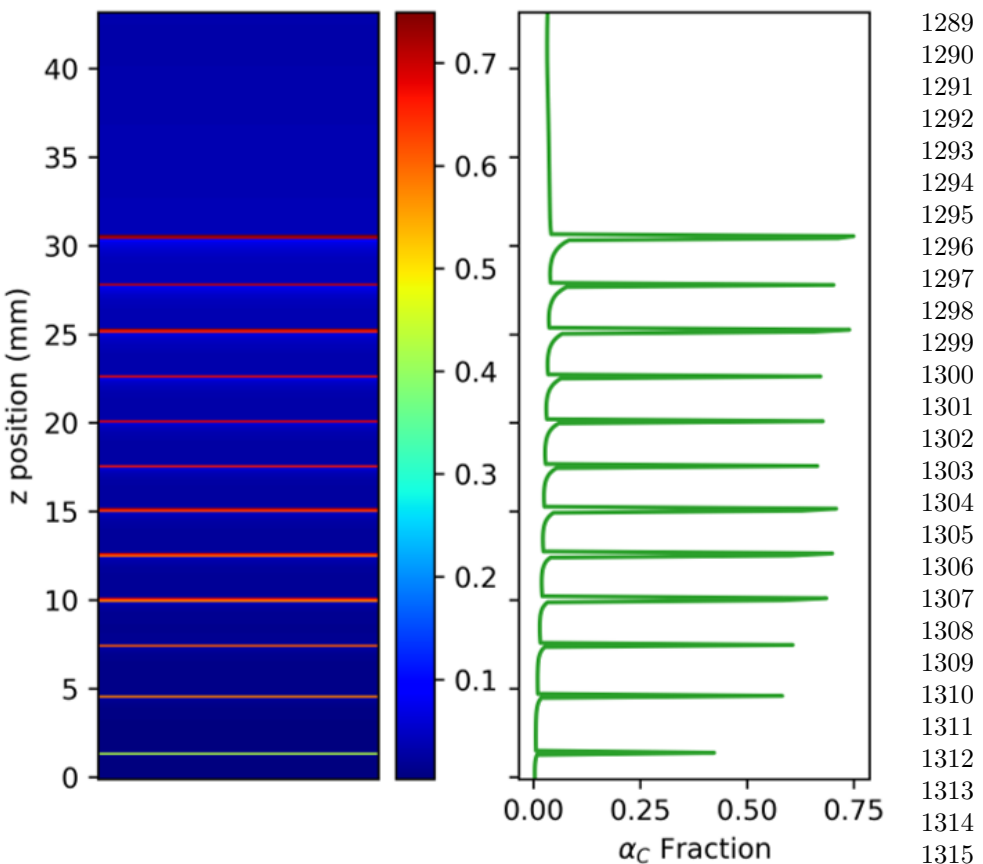


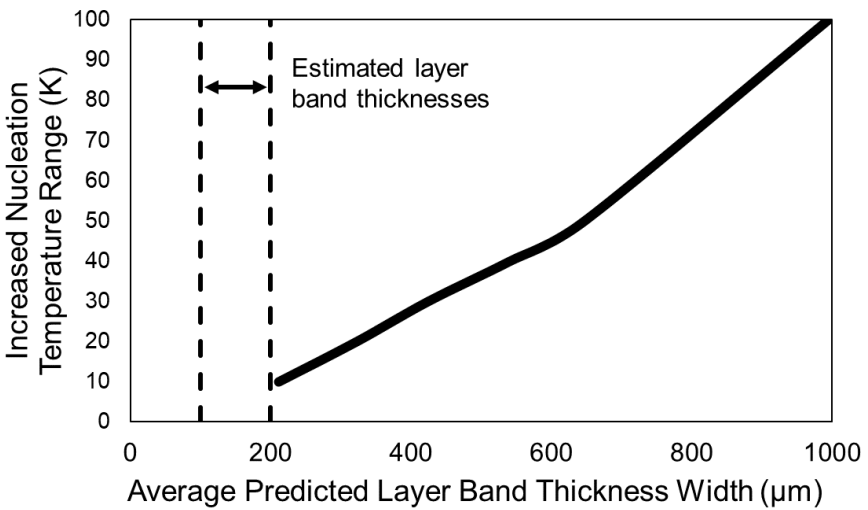
Fig. 13 1D vertical output of microstructural model, as in [Figure 12](#), but with a much wider range for the color bar. This result uses an increased nucleation site density under specific peak temperature conditions to accelerate growth of the α_C morphology, as in [Figure 10](#).

The relationship between the peak temperature range, which is a range of temperatures from T_β down, and predicted layer band thickness can be seen in [Figure 14](#). Peak widths were measured from microstructure model results at 20 % height for various peak temperature range assumptions. The thermal model used in these predictions had grid cells vertically spaced approximately 100 μm apart, negating the utility of further calculations resulting in lower predicted thicknesses of [Figure 14](#), as the results become strongly affected by

1289
1290
1291
1292
1293
1294
1295
1296
1297
1298
1299
1300
1301
1302
1303
1304
1305
1306
1307
1308
1309
1310
1311
1312
1313
1314
1315
1316
1317
1318
1319
1320
1321
1322
1323
1324
1325
1326
1327
1328
1329
1330
1331
1332
1333
1334

1335 discretization. However, given the quite small temperature range already indi-
 1336 cated, it is unlikely with all of the uncertainties present that further refinement
 1337 of the discretization would yield a more accurate result.
 1338

1340



1357

1358 **Fig. 14** Relationship between predicted layer band thicknesses and selected peak temper-
 1359 ature conditions under which acceleration of α_C growth occurs by increased nucleation site
 1360 density. Also shown dotted is the approximate observed layer band thicknesses.
 1361

1362

1363

1364 α_{BW} lath thicknesses, both predicted (blue) and measured (red) according
 1365 to Karra et al. [35] are shown in [Figure 15](#). The predicted fraction of α_C is
 1366 also shown at the right to provide location context for the thickness patterns
 1367 observed. The measured locations have been shifted slightly in order to more
 1368 closely match layer band locations with the predicted values in this plot, as
 1369 slight delays between deposition passes or other variables have slightly affected
 1370 the actual build locations.
 1371

1372

1373

1374

1375

1376

1377

1378

1379

1380

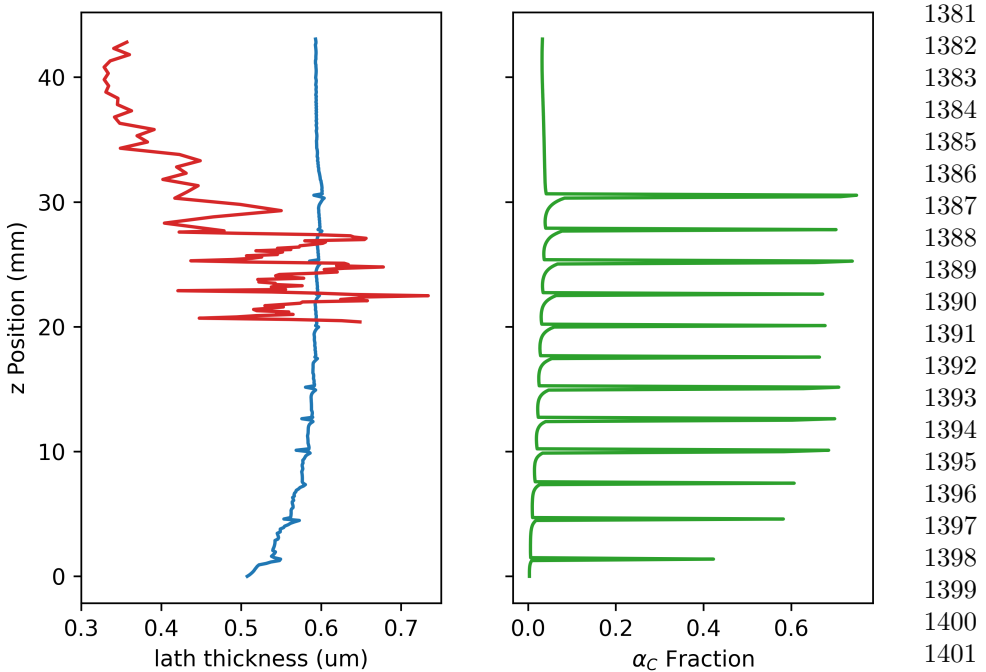


Fig. 15 Predicted α_{BW} lath thicknesses. Left panel shows predicted lath thicknesses in blue, with measured thicknesses according to Karra et al. [35] in red. Right panel shows α_C fraction in order to designate layer band locations for reference.

A zoomed-in view of lath thicknesses is shown in Figure 16, which corresponds to Line 2 in Figure 1. This is a convenient line because a high density of available images allows establishment of a good trend of lath thicknesses within three different layer bands and comparison with predicted trends from the model.

1381
1382
1383
1384
1385
1386
1387
1388
1389
1390
1391
1392
1393
1394
1395
1396
1397
1398
1399
1400
1401
1402
1403
1404
1405
1406
1407
1408
1409
1410
1411
1412
1413
1414
1415
1416
1417
1418
1419
1420
1421
1422
1423
1424
1425
1426

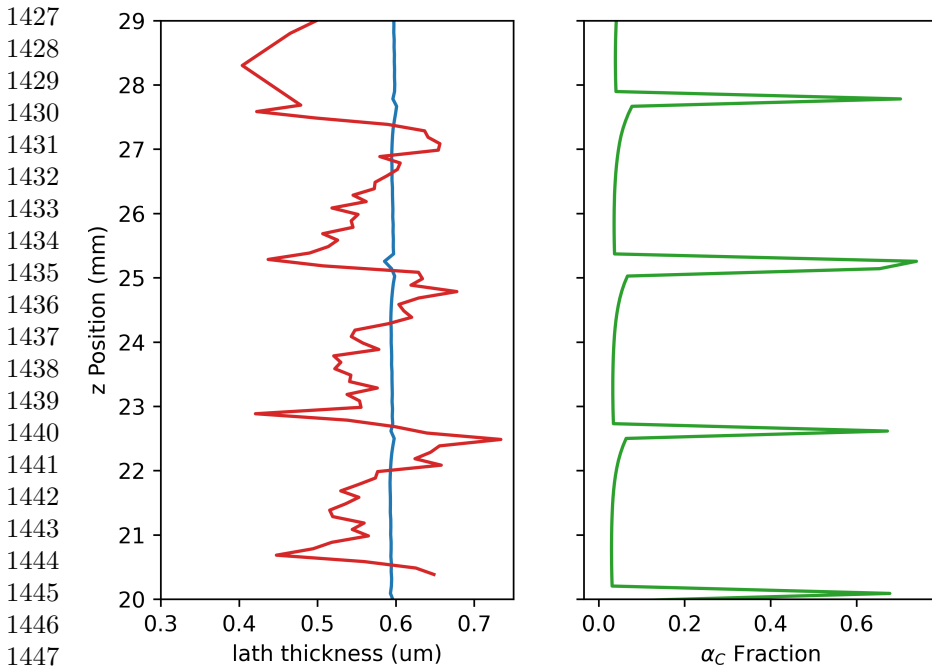


Fig. 16 Zoomed in view of Figure 15 showing a comparison of predicted values (blue) with measured values (red) along line 2 in Figure 1. Layer bands are mildly misaligned, likely due to differences in actual and modeled layer delays or other inaccuracies

5 Discussion

Previous modeling efforts [4–6, 11, 17] have focused on build scale predictions and achieved a useful level of accuracy in average values of phase fractions and lath thicknesses. However, they have not adequately explained or in some cases examined the differences between predictions and observed features on scales much less than 1 mm within DED builds with multi-millimeter scale beads.

Kelly [4] presented morphology fraction results on a sub-millimeter scale, but did not reproduce either the low fraction of α_C between layer bands or the nearly complete α_C microstructure of the bands themselves. The current

model accurately predicts these features. It also examined the lath thicknesses predictions based on the work of Charles [5, 6] on a smaller scale.

5.1 Phase and Phase Morphology Fraction Modeling

The focus of this study was generally in modeling phase morphology fractions, assuming that the values of total α/β were 91 %/9 % at room temperature. Thus, the term microstructure in this context generally refers to the morphology of the formed α phase. Observed microstructures were generally consistent with those seen in previous DED studies with similar scale and implied cooling and heating rates [2, 3, 5, 15, 18]. Periodic banding was observed with a primarily packet α_C microstructure, with most of the remainder of the build containing α_{BW} . This trend was well replicated on a build scale by the microstructure model, as can be seen in Figure 17 where a comparison of predicted α_C fraction is shown next to an optical image of the build. The correspondence in characteristic layers is quite good, with slight misalignment likely attributable to variable delay times between layer deposition, which have not been accounted for in the simulated thermal history, or to other minor thermal model inaccuracies.

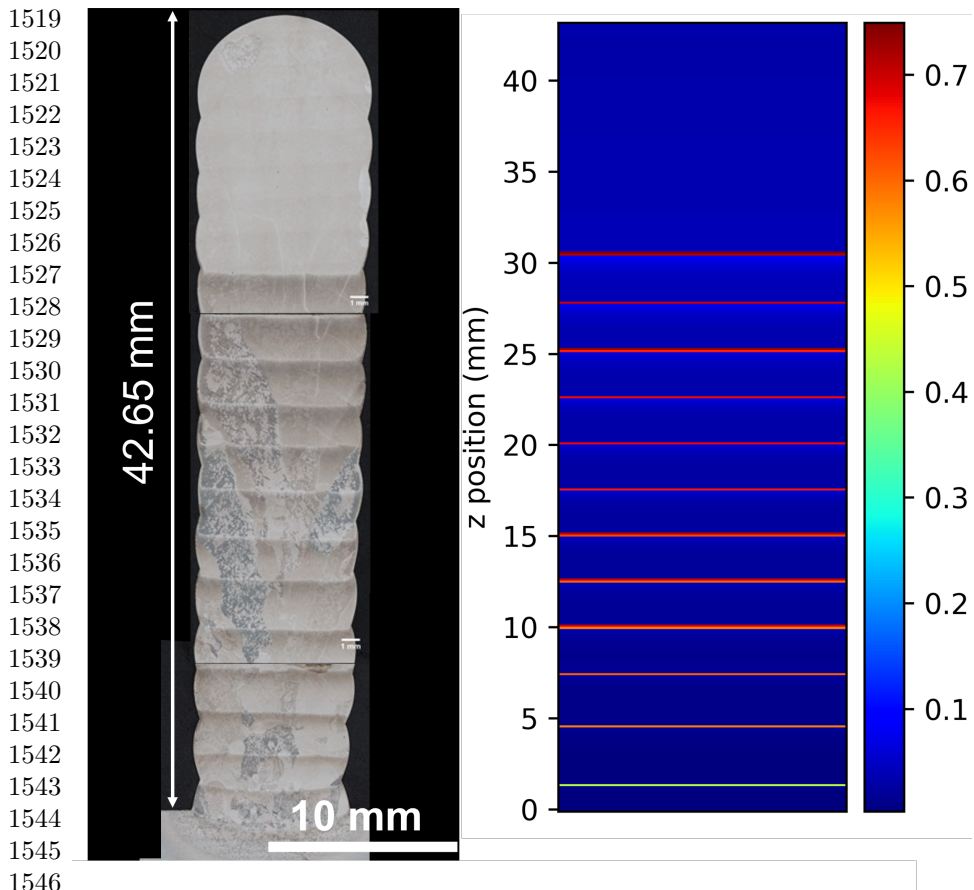


Fig. 17 Side by side comparison of actual and 1D model of build in this study. At the left is an optical build image and at the right is a predicted fraction of α_C .

1550

1551

1552 There was a gray-scale value (GSV) contrast in the optical image between
1553 the characteristic and transient regions which was not reflected in the predicted
1554 values. However, this was likely more a function of lath thickness rather than
1555 α morphology, with lighter gray-scale corresponding to smaller laths, as can
1556 be seen in Figure 18. The light bands of α_C correspond to the lower measured
1557 lath thickness values, which are similar to those seen in the transient region.
1558 Thus, while GSV is useful in delineating each characteristic layer, the mismatch
1559
1560
1561
1562
1563
1564

in transient region character in Figure 17 is not high when comparing model accuracy for phase morphology fractions.

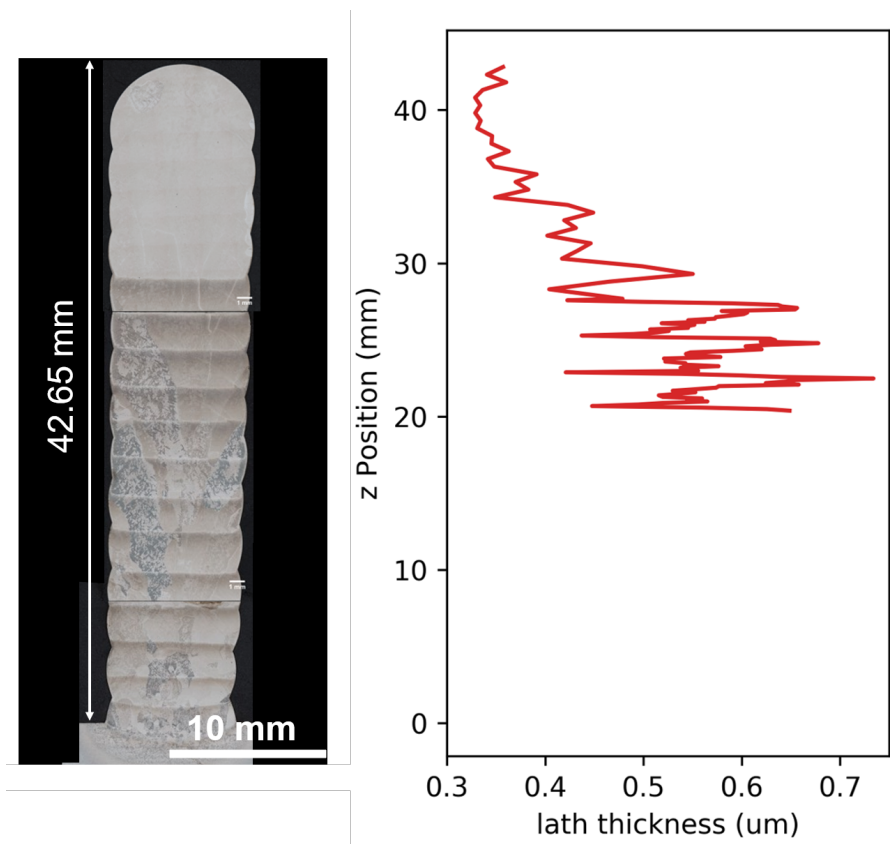
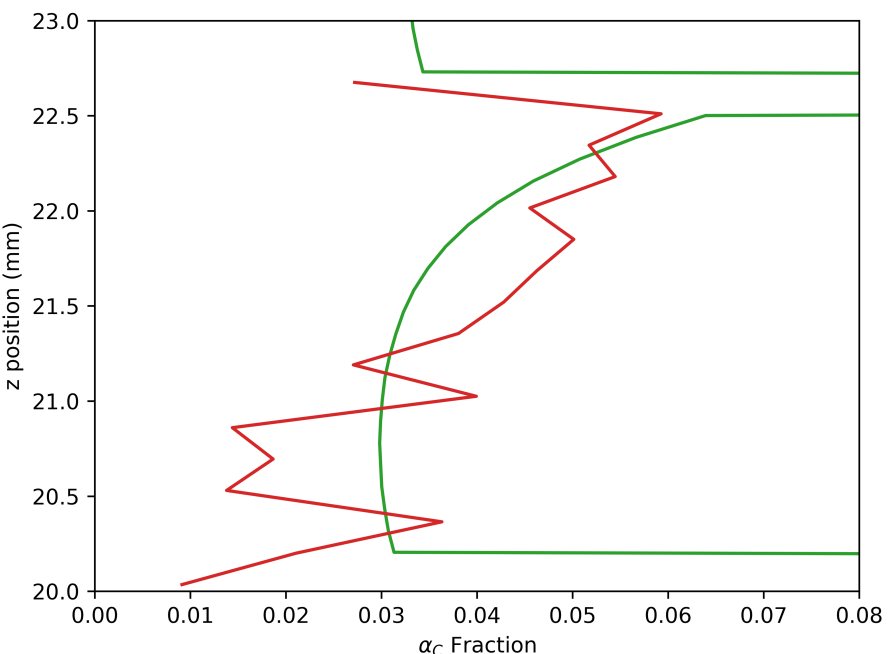


Fig. 18 Side by side comparison of optical image of stack and measured α lath thicknesses from Karra et al. [35]. Note that the variation in gray-scale is related to the measured lath thicknesses, with lower thicknesses resulting in higher (“brighter”) gray-scale values.

The nucleation and growth functions also generated results that agreed with observed microstructural trends on a fine scale, as can be seen in Figure 19. Here, a plot of estimated α_C growth across a characteristic layer is compared to predicted values. The function for α_C growth represented by the corresponding C-Curve in Figure 9, which is quite close to that of Kelly

1565
1566
1567
1568
1569
1570
1571
1572
1573
1574
1575
1576
1577
1578
1579
1580
1581
1582
1583
1584
1585
1586
1587
1588
1589
1590
1591
1592
1593
1594
1595
1596
1597
1598
1599
1600
1601
1602
1603
1604
1605
1606
1607
1608
1609
1610

1611 [2, 3], nicely predicted the increasing α_C morphology vertically between layer
 1612 bands. This may be a useful way to further examine and validate transforma-
 1613 tion curves in the future given the variety of cooling rates sampled by this
 1614 type of AM process.



1640 **Fig. 19** Predicted and estimated profile of α_C along the fourth characteristic layer down
 1641 from the transient region in [Figure 5](#). Red curve is estimated from measured width from
 1642 α_{GB} from Line 1 in [Figure 1](#) multiplied by estimated prior β grain boundaries across width.
 1643 Green curve is model prediction.

1644

1645
 1646
 1647 This trend of increasing α_C fraction moving up a characteristic layer was
 1648 a result of the next thermal cycle following the last excursion above T_β . The
 1649 temperature reached was high enough for significant dissolution of the α -phase.
 1650 Given the hierarchical posited nature of dissolution outlined in [subsubsection 3.3.3](#), α_C was preferentially retained and then allowed to regrow upon
 1651 subsequent cooling. This appears to fit the observed trend, supporting the
 1652

1653

1654

1655

1656

conclusion that this format for dissolution is reasonably correct for a practical model.

This effect can be seen directly in [Figure 20](#), a series of single point model outputs at points across the height of the characteristic layer considered in [Figure 19](#). All profiles of α and α_C are substantially the same until after Peak 1. Substantial divergence is revealed in Peak 2. At the bottom of the characteristic layer, temperature peak 2 is low enough that little α dissolution occurs, leaving only a small amount of β to transform to α_C on re-cooling. In contrast, significant α dissolves at the top of the characteristic layer and even more so in the band, leaving a far higher fraction of β to transform to α_C on re-cooling. This results in a progression of increasing α_C moving up the layer, as the temperatures of Peaks 3 and 4 are too low and result in too little α dissolution to change the morphology fractions, matching the trend in [Figure 19](#).

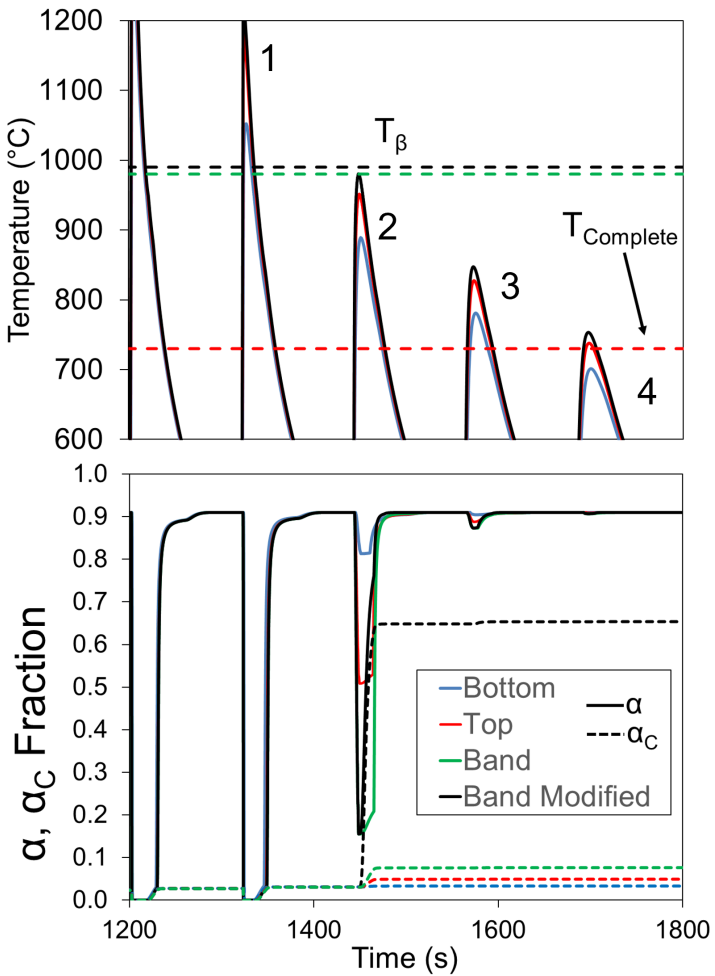


Fig. 20 Shared x-axis plot of temperature (top panel) and α development (bottom panel) with time for various positions in characteristic layer in Figure 19. In Figure 5, “Bottom” point *c*, “Top” is point *d* and “Band”/“Band Modified” are point *e*. For “Band”/“Band Modified”, the former was modeled with a higher α_C nucleation site density. Solid lines are total α and dotted lines are α_C . Points 1-4 represent temperature peaks of interest. The transus temperature (T_β), modeled range of band formation and the temperature at which the transformation is essentially complete ($T_{Complete}$) are shown.

1743
1744
1745
1746
1747
1748

It is important to note here that the kinetic function for α_C should change with β grain width since α_C grows from the α_{GB} - β interface. As the build progressed from bottom to top, grain selection eliminated many of the β variants present, significantly lowering the amount of prior β grain boundary present in any one cross section. This suggests that the C-curve for this morphology should be a function of prior β grain size, shifting right as the number of prior β grain boundaries decrease.

As there is of yet no model for β texture, changing α_C nucleation density based on texture is a planned future addition to the model. This would likely also help model accuracy by alleviating mismatches between observations and modeling results, such as those seen in [Figure 21](#). Running the model according to the C-Curves seen in [Figure 9](#) resulted in high α' fractions near the bottom of the stack, which were not observed. Increasing the nucleation site density of α_C , attributable to smaller grains, would effectively replace some or all of the α' with α_C .

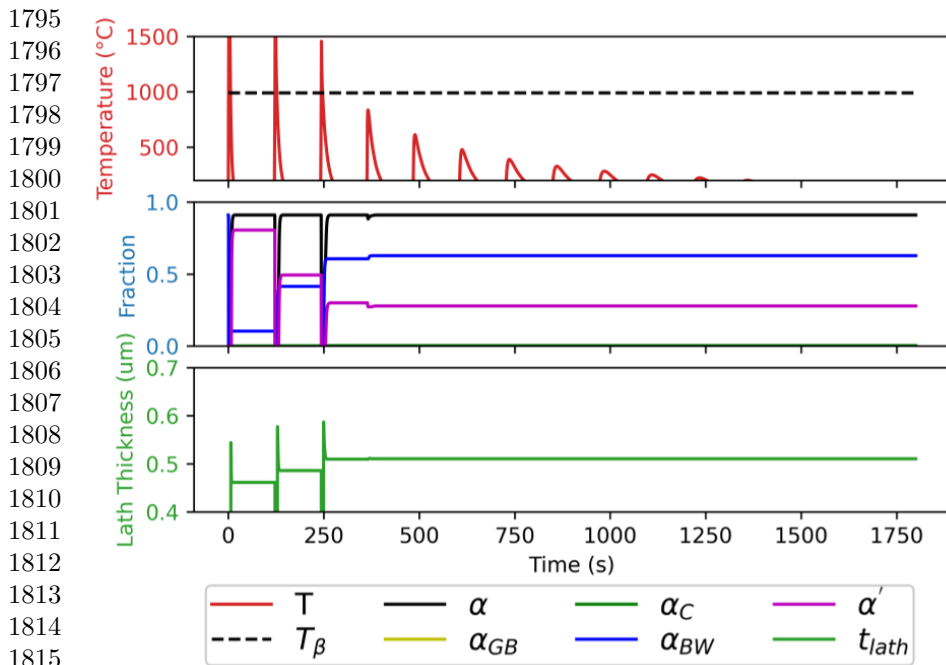


Fig. 21 Single-point model output at the bottom of the stack in Figure 5 showing large predicted α' fraction. This would be replaced or in part of completely by accelerating α_C reflecting smaller prior β grains near the build base.

An explanation for why α_C like microstructures were seen in the top of the transient region, as in Figure 8, is still missing. This type of microstructure in the same relative location was also observed by Baufeld et al. [15]. Cooling rates are still modeled to be high in this region, with few or no subsequent heating steps, so a primarily α_{BW} microstructure would be expected.

5.1.1 Modeling Layers Bands by Making α_C Kinetics

Mutable

Significant modifications were made to the framework laid out by Kelly [4] and Makiewicz [11] to accurately predict build scale changes in α morphology. The original kinetic function used by Kelly and adopted by Charles-Murgau

[5] and Irwin [17] did not accurately predict the magnitude of microstructural change present in the layer band features. As can be seen in Figure 12, simply using single curves for α_C and α_{BW} did not result in the nearly all packet α_C seen, instead resulting in values less than 10 %.

Using an increased nucleation site density in very particular locations corrected this error, as seen by comparing the “Band” and “Band Modified” curves in Figure 20. These locations were chosen based on the previous peak temperature occupying a particular range near the β transus, as shown. As argued by Ho et al. [18], for heating to within ≈ 30 K below the transus, significant α with a lamellar structure is likely retained, providing many additional parallel surfaces for α_C to grow from. This can be thought of as equivalent to reducing the grain size, which increases the amount of prior α - β interfacial area present per unit volume, shifting the α_C transformation curve to the left on a Time-Temperature-Transformation (TTT) diagram as shown in Figure 10. In the present model, this was accomplished by increasing the nucleation site density (N_0) in Equation 3, commensurately accelerating the kinetic function in Equation 2 and accelerating growth of α_C .

In this work, the ≈ 30 K range cited by Ho et al. [18] turned out to be too wide according to Figure 14. To replicate the scale of layer band features seen in the build, on the order of 100-200 μm , this range was reduced significantly to less than 10 K. Further refinement is limited by thermal model resolution and accuracy. It is also important to note that while this temperature range was taken to be starting from the β transus down, this does not need to be the case. If the described mechanism is applicable, the amount and distribution of α could be correct even if the transformation temperature were above the transus because of dissolution lag in the α to β reverse transformation. An estimation of dissolution lag in the reverse transformation is detailed by Kelly [3] and

1841
1842
1843
1844
1845
1846
1847
1848
1849
1850
1851
1852
1853
1854
1855
1856
1857
1858
1859
1860
1861
1862
1863
1864
1865
1866
1867
1868
1869
1870
1871
1872
1873
1874
1875
1876
1877
1878
1879
1880
1881
1882
1883
1884
1885
1886

1887 Elmer [47]. Whether this is the case or not, using a range just below the transus
1888 is still a reasonably practical approach because shifting the temperature range
1889 would not be noticeable given the limited spatial resolution.
1890

1891
1892

1893 **5.2 Lath Thickness Modeling**

1894

1895 There are some clear mismatches between the predictions from the model and
1896 observed trends in lath thicknesses. The characteristic and transient regions
1897 show a clear divergence in average lath thicknesses that are not replicated
1898 by simply assuming that an equilibrium lath thickness exists at each unique
1899 temperature, as the model outlined by Charles-Murgau [5] assumes. Cooling
1900 rates are similar enough in the two regions such that the overall predicted
1901 thicknesses from [Equation 12](#) in [Figure 15](#) are roughly the same in comparison
1902 with predictions at the upper end of the characteristic region. In the actual
1903 build, lath thicknesses in the transient region (at the top of the build) are
1904 clearly finer than those of the characteristic region except for those just above
1905 the layer bands. A plausible explanation is that all peak temperatures in the
1906 transient region remain significantly above T_β so the material only transformed
1907 once to α during final cooling, while the material in the characteristic region
1908 underwent more than one $\beta \rightarrow \alpha$ transformation.
1909

1910

1911 On the scale of the α lath spacing, far finer than the white bands, the pre-
1912 diction of constant thickness with increasing height within each characteristic
1913 layer is inconsistent to that observed, [Figure 16](#), with observations consistent
1914 with the results of Ho et al. [18] (see also a) and b) from [Figure 6](#)). Observed
1915 lath thicknesses increase with height through each characteristic layer, even
1916 though the cooling rates (as indicated by the prediction of lath thickness)
1917 are mostly consistent. This suggests that the mechanics of dissolution are
1918 important in lath thicknesses. This results in coarsening of laths when the
1919

1920

temperature peaks below T_β , which leads to the observed divide in average thicknesses between the characteristic and transient region.

5.3 Suggested Development

It was noted in the model physics from Kelly [4] that nucleation and growth of α_{BW} was too slow, with primary α_C growing from α_{GB} leading to a much larger predicted fraction than observed. Using the nucleation and growth functions from this study, the observed C-curve for α_{BW} has a nose much sharper than that used by Kelly [2, 3], with lower undercooling required for nucleation. Kelly reported values of grain boundary initiated α_C using this set of curves of up to 25-30%, while this study observed generally < 5 % in the middle region of the build. As previously mentioned, these higher α_C values may be realistic in regions of smaller grain size but the reported curves that Kelly derived from JMatPro do not replicate the patterns seen in the entire build.

A potential solution for this problem would be to shift the α_C curve to the right in Kelly's model, as well as using the slightly different curves in this study, which implies that TTT curves for Ti64 are not well understood. However, it seems reasonable to suppose that the α_C curve may depend on the available initiation site density. This motivates the study of β texture formation in DED builds, including coarsening with increasing height. The estimates of the α_C and α_{GB} nucleation site densities could be improved based on the β grain size. It could be argued that no nucleation barrier should be present for regrowth of α_C , as interfacial perturbation and growth may be all that is required, but this point is not vital in modeling the current process as long as the nucleation barrier used is low enough.

The lath thickness model proposed by Charles [5, 6] and adopted by Irwin [17] also proved useful at the scale of the build. Although the values used in

1933
1934
1935
1936
1937
1938
1939
1940
1941
1942
1943
1944
1945
1946
1947
1948
1949
1950
1951
1952
1953
1954
1955
1956
1957
1958
1959
1960
1961
1962
1963
1964
1965
1966
1967
1968
1969
1970
1971
1972
1973
1974
1975
1976
1977
1978

1979 this study ([Table II](#)) were different from those of Irwin [[17](#)] (adopted also by
 1980 Charles-Murgau [[5](#)]), this is likely a consequence of applying a stereological cor-
 1981 rection to the lath thickness determination [[35](#)] rather than gross physical build
 1982 differences. [Figure 15](#) shows agreement on a build scale between predicted and
 1983 measured lath thicknesses, but further understanding of coarsening patterns
 1984 observed in characteristic layers and the differences between the characteristic
 1985 and transient regions is needed.

1990 Work is also needed to address dissolution effects on lath sizes, as pro-
 1991 posed by Charles-Murgau [[5, 6](#)] to improve the match between simulated and
 1992 measured lath spacings. Below the β transus, smaller laths may preferentially
 1993 revert to β during heating. Larger laths may be retained and perhaps coarsen,
 1994 which would result in larger lath sizes than those modeled. This might effec-
 1995 tively reverse the as-formed size distribution, with the latest forming laths
 1996 dissolved first. Potential refinements may also address the nucleation physics,
 1997 particularly site densities or activation energies, changing with prior thermal
 1998 peak heights.

1999 The current model considers each diffusional morphology separately since
 2000 the initiation mechanisms, as detailed in [subsubsection 3.3.5](#), are likely differ-
 2001 ent. α_{BW} dominates in the deposition method, so the α_{BW} lath thickness is
 2002 a reasonable focus in this work. To deal with more significant fractions of α_C
 2003 near the base metal where the prior β grain size is much smaller, a two part
 2004 lath prediction model, with different fits for α_C and α_{BW} , may be beneficial
 2005 because of the differing initiation mechanisms of each morphology.

2006

2007 6 Conclusion

2008

2009 Single-stacked Ti64 from welding scale DED processes results in builds with
 2010 two regions, a lower region of cyclical brightness, *i.e.*, a series of bands whose
 2011

locations are only indirectly related to the beads, and an upper region of uniform appearance in optical microscopy. Inset amongst the predominantly $\alpha+\beta$ basketweave microstructure, each band is delineated by a narrow region that is closer to a colony microstructure. The aligned laths in the colony microstructure of each band are relatively bright in optical micrographs, likely because of their smaller width, which explains the designation of “white bands” in the literature.

In this study, a microstructural evolution model for rapidly cooled LWD Ti64 based on a multiphase JMAK approach has been developed. Improvements over prior models include modifications to the kinetic functions through nucleation and growth functions, and modification of the α_C phase physics to account for layer bands and lath spacing. These modifications allowed for a better agreement on a small scale compared to previous studies and reasonable prediction of layer bands. Importantly, their necessity in this study also strongly suggests that the α_C kinetic function must be considered mutable not only from grain size, but also from thermal history. This indicates that prediction of microstructural development at the scale of features that control strength, for example, is feasible provided that enough of the physics of the phase transformation is included.

Acknowledgments. This work was supported by both the Quality Made program led by Lockheed Martin under prime contract N00014-18-C-1026 from the Office of Naval Research and the National Aeronautics and Space Administration (NASA) Space Technology Research Institute (STRI) program under grant 80NSSC23K1342.”. Glynn Adams, Ed Pierson, Brandon Abranovic, Elizabeth Chang-Davidson, as well as Profs. David Laughlin, Peter Collins, and Jack Beuth are thanked for fruitful discussions. The authors acknowledge also

2025
2026
2027
2028
2029
2030
2031
2032
2033
2034
2035
2036
2037
2038
2039
2040
2041
2042
2043
2044
2045
2046
2047
2048
2049
2050
2051
2052
2053
2054
2055
2056
2057
2058
2059
2060
2061
2062
2063
2064
2065
2066
2067
2068
2069
2070

2071 use of the Materials Characterization Facility at Carnegie Mellon University
2072 supported by in part under grant MCF-677785.
2073

2074
2075 **Conflict of Interest.** The authors declare that they have no conflict of
2076 interest.
2077

2078

2079 **References**
2080

2081
2082 [1] Liu, S., Shin, Y.C. Materials and Design **164**, 107552 (2019). <https://doi.org/10.1016/j.matdes.2018.107552>
2083

2084
2085 [2] Kelly, S.M., Kampe, S.L. Metallurgical and Materials Transactions A:
2086 Physical Metallurgy and Materials Science **35** A(6), 1861–1867 (2004).
2087
2088 <https://doi.org/10.1007/s11661-004-0095-7>
2089

2090
2091 [3] Kelly, S.M., Kampe, S.L. Metallurgical and Materials Transactions A
2092
2093 [4] Kelly, S.M.: Thermal and microstructure modeling of metal deposition
2094 processes with application to Ti-6Al-4V. PhD thesis, Virginia Polytechnic
2095 Institute and State University (2004). <http://hdl.handle.net/10919/29731>
2096

2097
2098
2099
2100
2101
2102
2103
2104 [5] Charles Murgau, C.: Microstructure model for Ti-6Al-4V used in simula-
2105 tion of additive manufacturing. Doctor of philisophy, Lulea University of
2106
2107 Technology (2016)
2108

2109
2110 [6] Charles, C.: Modelling microstructure evolution of weld deposited ti-6al-
2111 4v. Licentiate thesis, Lulea University of Technology (2008). <https://doi.org/10.1402-1757>. <http://epubl.ltu.se/1402-1757/2008/47/LTU-LIC-0847-SE.pdf>
2112
2113
2114
2115
2116

- [7] Charles, C., Järvstråt, N.: Development of a microstructure model for metal deposition of titanium alloy Ti-6Al-4V. In: Ninomi, M., Akiyama, S., Ikeda, M., Hagiwara, M., Maruyama, K. (eds.) 11th World Conference on Titanium (Ti-2007), pp. 1201–1204. The Japan Institute of Metals, Kyoto, Japan (2007) 2117
2118
2119
2120
2121
2122
2123
2124
2125
- [8] Charles, C., Järvstråt, N.: Modelling Ti-6Al-4V microstructure by evolution laws implemented as finite element subroutines: Application to TIG metal deposition. In: ASM Proceedings of the International Conference: Trends in Welding Research, pp. 477–485. ASM International, Pine Mountain, Georgia (2009). <https://doi.org/10.1361/cp2008twr477> 2126
2127
2128
2129
2130
2131
2132
2133
2134
2135
2136
2137
2138
2139
2140
- [9] Charles Murgau, C., Pederson, R., Lindgren, L.-E. Modelling and Simulation in Materials Science and Engineering **20**(5) (2012). <https://doi.org/10.1088/0965-0393/20/5/055006> 2141
2142
2143
2144
2145
2146
2147
2148
2149
2150
2151
2152
2153
2154
2155
2156
- [10] Charles Murgau, C., Lundbäck, A., Åkerfeldt, P., Pederson, R. Materials **12**(21), 3534 (2019). <https://doi.org/10.3390/ma12213534> 2157
2158
2159
2160
2161
2162
- [11] Makiewicz, K.T.: Development of simultaneous transformation kinetics microstructure model with application to laser metal deposited Ti-6Al-4V and alloy 718. MS Thesis, The Ohio State University (2013). http://rave.ohiolink.edu/etdc/view?acc_num=osu1366023857
- [12] Baufeld, B., Van Der Biest, O. Science and Technology of Advanced Materials **10**(1) (2009). <https://doi.org/10.1088/1468-6996/10/1/015008>
- [13] Baufeld, B., Van Der Biest, O., Gault, R. International Journal of Materials Research **100**(11) (2009). <https://doi.org/10.3139/146.110217>
- [14] Baufeld, B., der Biest, O.V., Gault, R. Materials and Design **31**(SUPPL.

- 2163 1), 106–111 (2010). <https://doi.org/10.1016/j.matdes.2009.11.032>
2164
2165 [15] Baufeld, B., Brandl, E., Van Der Biest, O. Journal of Materials Processing
2166 Technology **211**(6), 1146–1158 (2011). <https://doi.org/10.1016/j.jmatprotec.2011.01.018>
2169
2170
2171 [16] Baufeld, B., Van Der Biest, O., Gault, R., Ridgway, K. IOP Conference
2172 Series: Materials Science and Engineering **26**(1) (2011). <https://doi.org/10.1088/1757-899X/26/1/012001>
2175
2176
2177 [17] Irwin, J., Reutzel, E.W., Michaleris, P., Keist, J., Nassar, A.R. Journal
2178 of Manufacturing Science and Engineering, Transactions of the ASME
2179 **138**(11), 1–11 (2016). <https://doi.org/10.1115/1.4033525>
2181
2182
2183 [18] Ho, A., Zhao, H., Fellowes, J.W., Martina, F., Davis, A.E., Prangnell,
2184 P.B. Acta Materialia **166**, 306–323 (2019). <https://doi.org/10.1016/j.actamat.2018.12.038>
2186
2187
2188
2189 [19] Ahmed, T., Rack, H.J. Materials Science and Engineering A **243**(1-2),
2190 206–211 (1998). [https://doi.org/10.1016/s0921-5093\(97\)00802-2](https://doi.org/10.1016/s0921-5093(97)00802-2)
2191
2192
2193 [20] Oh, S.A., Lim, R.E., Aroh, J.W., Chuang, A.C., Gould, B.J., Amin-
2194 Ahmadi, B., Bernier, J.V., Sun, T., Pistorius, P.C., Suter, R.M., Rollett,
2195 A.D. Materials Research Letters **9**(10), 429–436 (2021). <https://doi.org/10.1080/21663831.2021.1966537>
2196
2197
2198
2199
2200 [21] Avrami, M. The Journal of Chemical Physics **7**(12), 1103–1112 (1939).
2201
2202 <https://doi.org/10.1063/1.1750380>
2203
2204
2205 [22] Avrami, M. The Journal of Chemical Physics **8**(2), 212–224 (1940). <https://doi.org/10.1063/1.1750631>
2206
2207
2208

- [23] Avrami, M. *The Journal of Chemical Physics* **9**(2), 177–184 (1941). <https://doi.org/10.1063/1.1750872> 2209
2210
2211
2212
- [24] Johnson, W.A., Mehl, R.F. *Transactions of the American Institute of Mining and Metallurgical Engineers* **135**, 416–442 (1939) 2213
2214
2215
2216
- [25] Kolmogorov, A.N. *Izv. Akad. Nauk SSSR Ser. Mat.*(3), 355–359 (1937) 2217
2218
2219
- [26] Grong, Ø.: *Metallurgical Modelling of Welding*, 2nd edn. The Institute of Materials, London (1997). <https://doi.org/10.1002/maco.19970480319> 2220
2221
2222
2223
- [27] Grong, Ø., Shercliff, H.R. *Progress in Materials Science* **47**(2), 163–282 (2002). [https://doi.org/10.1016/S0079-6425\(00\)00004-9](https://doi.org/10.1016/S0079-6425(00)00004-9) 2224
2225
2226
2227
- [28] Cahn, J.W. *Acta Metallurgica* **4**(6), 572–575 (1956). [https://doi.org/10.1016/0001-6160\(56\)90158-4](https://doi.org/10.1016/0001-6160(56)90158-4) 2228
2229
2230
2231
- [29] Christian, J.W.: *The Theory of Transformations in Metals and Alloys*, 3rd edn. Elsevier Science Ltd, Oxford, UK (2002) 2232
2233
2234
2235
- [30] Arcella, F.G., Froes, F.H. *Jom* **52**(5), 28–30 (2000). <https://doi.org/10.1007/s11837-000-0028-x> 2236
2237
2238
2239
- [31] Saunders, N., Guo, Z., Li, X., Miodownik, A.P., Schillé, J.P. *Journal of Materials* **55**(12), 60–65 (2003). <https://doi.org/10.1007/s11837-003-0013-2> 2240
2241
2242
2243
2244
2245
- [32] Vander Voort, G.F. *Industrial Heating* **73**(8), 77–84 (2006) 2246
2247
- [33] ASTM: E112-12:Standard Test Methods for Determining Average Grain Size. Technical report (2012). <https://doi.org/10.1520/E0112-12.1.4> 2248
2249
2250
2251
2252
- [34] Rueden, C.T., Schindelin, J., Hiner, M.C., DeZonia, B.E., Walter, A.E., 2253
2254

50 *LWD Phase Transformations in Ti64*

- 2255 Arena, E.T., Eliceiri, K.W. BMC Bioinformatics **18**(1), 1–26 (2017) <https://arxiv.org/abs/1701.05940>. <https://doi.org/10.1186/s12859-017-1934-z>
- 2256
- 2257
- 2258
- 2259 [35] Karra, V.S.S.A., Verma, A.K., Guzel, A., Huck, A., Rollett, A.D. Mate-
2260 rials Characterization **186**, 111802 (2022). <https://doi.org/10.1016/j.matechar.2022.111802>
- 2261
- 2262
- 2263
- 2264
- 2265 [36] Van Rossum, G., Drake Jr., F.L.: Python 3 Reference Manual. CreateS-
2266 pace, Scotts Valley, CA (2009)
- 2267
- 2268
- 2269 [37] Boivineau, M., Cagran, C., Doytier, D., Eyraud, V., Nadal, M.-H.,
2270 Wilthan, B., Pottlacher, G. International Journal of Thermophysics
2271 **27**(2), 507–529 (2006). <https://doi.org/10.1007/PL00021868>
- 2272
- 2273
- 2274
- 2275 [38] Sunderland, J.E., Johnson, K.R. ASHRAE Transactions **70**, 237–241
2276 (1964)
- 2277
- 2278
- 2279 [39] Mills, K.C.: Recommended Values of Thermophysical Properties for
2280 Selected Commercial Alloys. Woodhead Publishing Limited on behalf of
2281 ASM International, Cambridge, UK (2002)
- 2282
- 2283
- 2284
- 2285 [40] Koistinen, D.P., Marburger, R.E. Acta Metallurgica **7**(1), 59–60 (1959).
2286 [https://doi.org/10.1016/0001-6160\(59\)90170-1](https://doi.org/10.1016/0001-6160(59)90170-1)
- 2287
- 2288
- 2289 [41] Andersson, J.O., Helander, T., Hoglund, L., Shi, P.F., Sundman, B.:
2290 Thermo-Calc and DICTRA, Computational tools for materials science.,
2291 TCFE9 Database. Calphad (2002)
- 2292
- 2293
- 2294
- 2295 [42] Jones, S.J., Bhadeshia, H.K.D.H. Acta Materialia **45**(7), 2911–2920
2296 (1997)
- 2297
- 2298
- 2299 [43] Whelan, M.J. Metal Science Journal **3**(1), 95–97 (1969). <https://doi.org/10.1007/BF02911111>
- 2300

10.1179/msc.1969.3.1.95	2301
	2302
[44] Fujii, H.: Continuous cooling transformation characteristics of α + β titanium alloys. Technical Report 62 (1994)	2303
	2304
	2305
	2306
	2307
[45] Sun, Z., Guo, S., Yang, H. Acta Materialia 61 (6), 2057–2064 (2013). https://doi.org/10.1016/j.actamat.2012.12.025	2308
	2309
	2310
	2311
[46] Gil, F.J., Ginebra, M.P., Manero, J.M., Planell, J.A. Journal of Alloys and Compounds 329 (1-2), 142–152 (2001). https://doi.org/10.1016/S0925-8388(01)01571-7	2312
	2313
	2314
	2315
	2316
[47] Elmer, J.W., Palmer, T.A., Babu, S.S., Zhang, W., DebRoy, T. Journal of Applied Physics 95 (12), 8327–8339 (2004). https://doi.org/10.1063/1.1737476	2317
	2318
	2319
	2320
	2321
	2322
[48] Porter, D.A., Easterling, K.E.: Phase Transformations in Metals and Alloys, 2nd edn., pp. 263–282. CRC Press, Boca Raton, FL (2004)	2323
	2324
	2325
	2326
[49] Kozeschnik, E., Janssens, K.G.F., Raabe, D., Miodownik, M.A., Nestler, B.: Computational Materials Engineering, 1st edn., pp. 28–30. Elsevier, Amsterdam, Netherlands (2007). https://doi.org/10.1016/B978-0-12-369468-3.X5000-X . https://linkinghub.elsevier.com/retrieve/pii/B9780123694683X5000X	2327
	2328
	2329
	2330
	2331
	2332
	2333
	2334
	2335
	2336
[50] Lukas, H., Fries, S.G., Sundman, B.: Computational Thermodynamics: The CALPHAD Method, 1st edn., pp. 33–34. Cambridge University Press, Cambridge, UK (2007)	2337
	2338
	2339
	2340
	2341
	2342
[51] Hillert, M.: Phase Equilibria, Phase Diagrams and Phase Transformations, 2nd editio edn., pp. 142–143. Cambridge University Press,	2343
	2344
	2345
	2346

2347 Cambridge, UK (2008)

2348

2349 [52] Semiatin, S.L., Brown, T.M., Goff, T.A., Fagin, P.N., Barker, D.R.,
 2350 Turner, R.E., Murry, J.M., Miller, J.D., Zhang, F. Metallurgical and
 2351 Materials Transactions A: Physical Metallurgy and Materials Science **35**
 2352 **A**(9), 3015–3018 (2004). <https://doi.org/10.1007/s11661-004-0250-1>
 2353

2354 **A Appendix: Model Physics Details**

2355 **A.1 Heterogeneous Nucleation Model**

2356 In [Equation 3](#), Q is the energy barrier for nucleation ([Equation A1](#)), and N_0 is
 2357 the number of nucleation sites per unit volume per unit time. The dependence
 2358 on contact angle (θ) is taken from Porter and Easterling [\[48\]](#).
 2359

$$2360 Q_{het} = \frac{16\pi\gamma_{\alpha\beta}^3}{3(\Delta G_V + \Delta G_S)^2} \frac{(2 + \cos(\theta))(1 - \cos(\theta))^2}{2} \quad (A1)$$

2361 Temperature dependent driving forces for nucleation (ΔG_V) were derived
 2362

2363 from the Thermo-Calc software [\[41\]](#) using the TCTI2 database and a basic
 2364 90Ti-6Al-4V composition. Importantly, the HCP α phase was rendered dor-
 2365 mant in Thermo-Calc to allow for formation of non-equilibrium compositions
 2366 2367 commensurate with true nucleation driving forces [\[49, 50\]](#). This is essentially
 2368 the parallel tangent approach outlined in Porter and Easterling [\[48\]](#), or Hillert
 2369 [\[51\]](#), finding the tangent to the ΔG_β curve at the alloy composition and maxi-
 2370 2371 mizing the difference to the ΔG_α curve using a parallel tangent. This results in
 2372 2373 the driving force curve intersecting the energy axis at the transus, rather than
 2374 2375 well below as modeled by Makiewicz [\[11\]](#) and shown in [Figure A1](#). Extracted
 2376 2377 values were then curve-fitted with a sixth-order piece-wise polynomial for
 2378 2379 Python implementation, which was the approach for all extracted Thermo-Calc
 2380 2381 data necessary for this model.
 2382

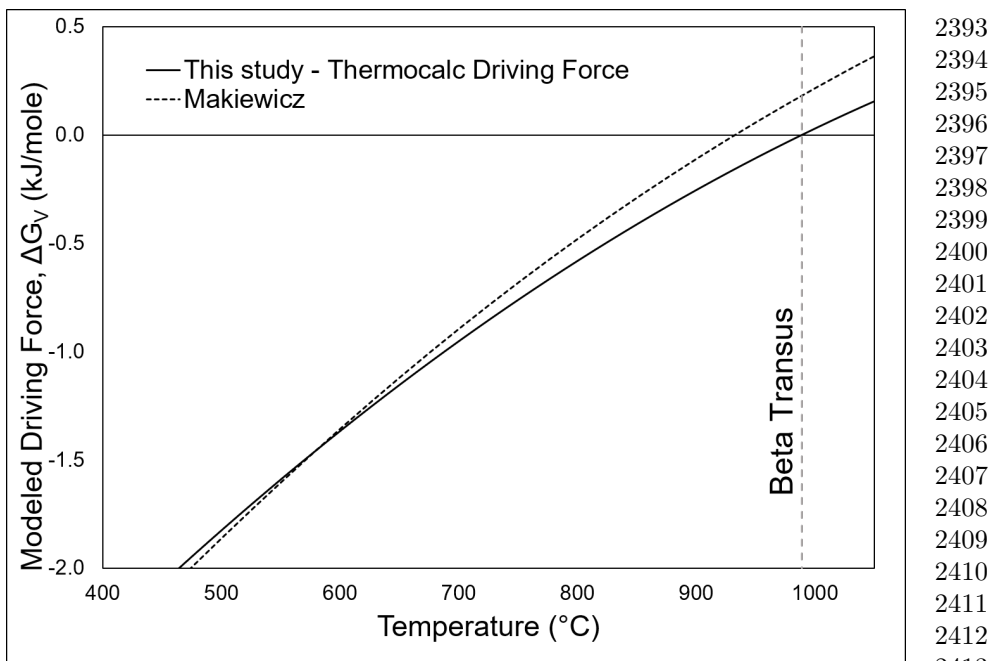


Fig. A1 Nucleation driving forces calculated from Thermo-Calc by different methods shown along with the Beta Transus [11]

Initial estimates of the contact angles (θ) between the α and β phases were obtained from Thermo-Calc TCTI2 [41] and were used as a fitting parameter. Strain energies (ΔG_S) were estimated starting from the values used by Makiewicz, but were ultimately used as a tuning parameter particularly to inhibit α_{BW} formation at higher temperatures. Interphase surface energy ($\gamma_{\alpha\beta}$) was estimated at 0.01 J/m^2 based on Thermo-Calc values.

A.2 Diffusional Growth Model

A temperature dependent parabolic growth rate (ν) based on the Zener approximation from Porter and Easterling [48] was used to model the growth of the α phase, with the resulting radius (r) shown in [Equation 4](#). This assumes planar growth, but as Porter and Easterling describe, it should be adequate

2393
2394
2395
2396
2397
2398
2399
2400
2401
2402
2403
2404
2405
2406
2407
2408
2409
2410
2411
2412
2413
2414
2415
2416
2417
2418
2419
2420
2421
2422
2423
2424
2425
2426
2427
2428
2429
2430
2431
2432
2433
2434
2435
2436
2437
2438

54 *LWD Phase Transformations in Ti64*

2439 for growth of a curved interface as well and hence this simple format has been
2440 used. Correcting for lamellar growth was not attempted; it would likely require
2441 additional assumptions.
2442

2443 Vanadium in the β phase was assumed to be the diffusion limiting element
2444 based on the work of Kelly [3] and Gil et al. [46] and was accordingly consid-
2445 ered the element of interest for growth. X_{V_0} was considered to be the molar
2446 bulk alloy composition ($\approx 3.6\%$) and X_{V_α} and X_{V_β} were considered to be
2447 the interfacial vanadium compositions on the α and β sides of the interface,
2448 respectively. Interfacial equilibrium was assumed, leading to equilibrium val-
2449 ues of vanadium in the respective phases at the interface. Equilibrium data for
2450 vanadium in each phase was derived from the Thermo-Calc software TCTI2
2451 database [41] and curve fitted. Results can be seen in [Figure A2](#). The diffusiv-
2452 ity of vanadium (D_V) was assumed to follow [Equation A2](#) based on Semiatin
2453 et al. [52].
2454

$$D_V = 1 * 10^{-7} e^{\frac{17460}{T}} \frac{m^2}{s} \quad (\text{A2})$$

2455
2456
2457
2458
2459
2460
2461
2462
2463
2464
2465
2466
2467
2468
2469
2470
2471
2472
2473
2474
2475
2476
2477
2478
2479
2480
2481
2482
2483
2484

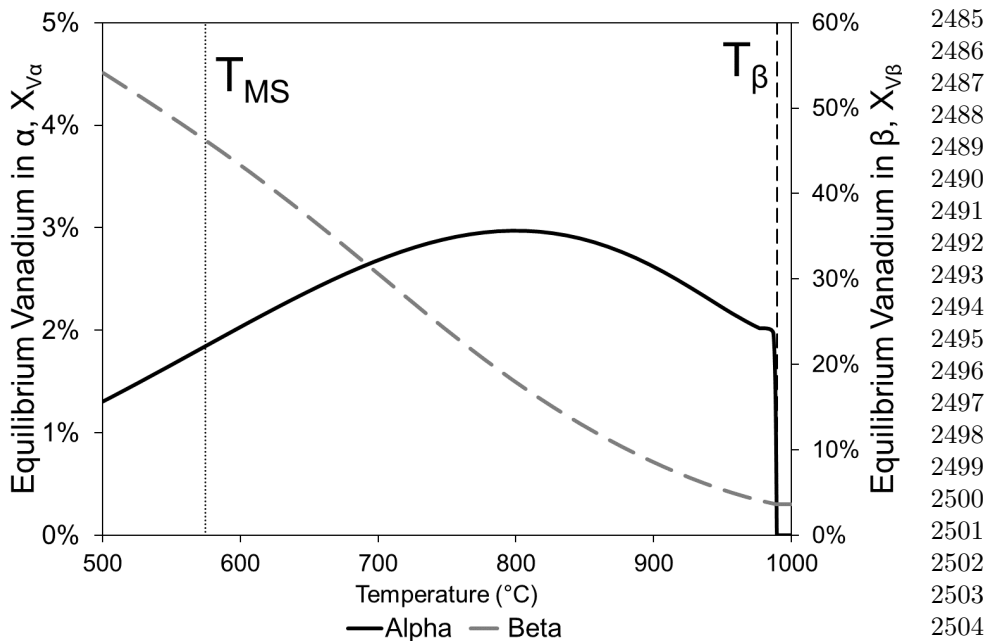


Fig. A2 Temperature dependent equilibrium vanadium compositions in the α and β phases calculated from Thermo-Calc TCTI2 database.

Nucleation and growth rates were then inserted into [Equation 2](#), with the result used in [Equation 1](#) to estimate the extent of β transformed to α in a time step.

A.3 Diffusionless Transformation

A diffusionless martensitic transformation was also modeled in this study. The Martensite start temperature (T_{MS}) was assumed to be 848 K, based on the findings of Murgau-Charles [5] from a literature survey. The massive phase transformation was ignored for the purposes of this study. Above the martensite start temperature, diffusional phase changes were allowed to occur as outlined above. Below this temperature, diffusionless transformation following a Koistinen-Marburger [40] type equation was allowed to occur, rapidly

2485
2486
2487
2488
2489
2490
2491
2492
2493
2494
2495
2496
2497
2498
2499
2500
2501
2502
2503
2504
2505
2506
2507
2508
2509
2510
2511
2512
2513
2514
2515
2516
2517
2518
2519
2520
2521
2522
2523
2524
2525
2526
2527
2528
2529
2530

2531 converting any remaining β above the equilibrium value to α' . The form of
2532 this can be seen in [Equation 5](#), where ζ' represents the fraction of martensite
2533 transformed at a specified temperature and is assumed to be time indepen-
2534 dent. Importantly, this has been modified from the original format with X_β
2535 to reflect the incomplete nature of this transformation, as compared to the
2536 complete nature of the austenite-martensite transformation from the origi-
2537 nal paper. This quantity represents the fraction of β that is remaining to be
2538 transformed, meaning the remaining beta fraction excluding the calculated
2539 temperature dependent equilibrium value. The value of C_{MB} is a fitting con-
2540 stant for specific material systems, with units of 1/K. In steels, Koistenin and
2541 Marburger found this value to be approximately 1.1×10^{-2} . Murgau-Charles
2542 [5] investigated a range of values for Ti64 and concluded that a value between
2543 3×10^{-3} and 5×10^{-3} was reasonable. The lower value was selected for this study.
2544
2545
2546

2547 A.4 Calculation of $V_{eq-\alpha}$

2548 Equilibrium α ($V_{eq-\alpha} = \alpha_{eq}$) values were again derived from the Thermo-Calc
2549 software[41] and curve fitted for programmatic implementation. Thermo-Calc
2550 predicts a roughly 97 % α_{eq} fraction at room temperature, with the phase
2551 comprised of nearly pure vanadium. This result is not observed in AM builds,
2552 with a room temperature fraction of roughly 91 % α_{eq} typically reported,
2553 perhaps because of the kinetic barrier of vanadium diffusion required to reach
2554 such high concentrations. Kelly [3] recommended adjustment of the equilibrium
2555 curve to reflect this reality. For this study, the Thermo-Calc derived curve was
2556 adjusted to a constant 91 % α_{eq} at temperatures below 727 °C (1000 K), as
2557 there is little deviation in the curve and transformation is essentially complete
2558 below this temperature. Above this temperature, α_{eq} was adjusted by scaling
2559 the curve to reflect a 91 % maximum by [Equation A3](#).
2560
2561

$$\alpha_{eq-adjusted} = 0.91 \frac{\alpha_{eq}}{\alpha_{eq-max}} \quad (\text{A3})$$

The (α_{eq}) curve derived from Thermo-Calc are shown in [Figure A3](#), along with the adjusted curve.

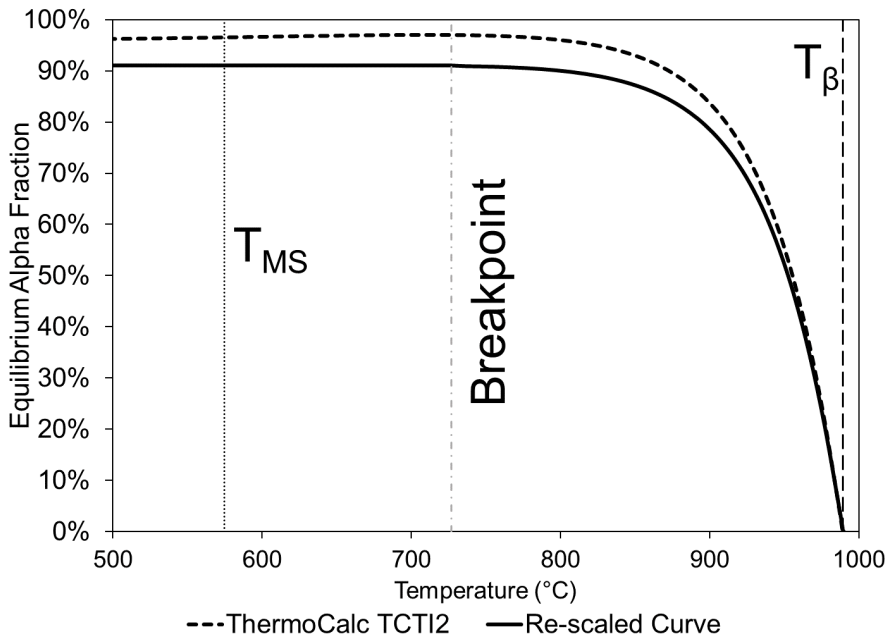


Fig. A3 α_{eq} curve calculated from Thermo-Calc TCTI2 database, along with adjusted curve scaled to 91% relative maximum for room temperature microstructure. Also shown are the β transus, T_{MS} , and the breakpoint for the fitting function, with a fit above and a constant 91 % α_{eq} below.

2577
2578
2579
2580
2581
2582
2583
2584
2585
2586
2587
2588
2589
2590
2591
2592
2593
2594
2595
2596
2597
2598
2599
2600
2601
2602
2603
2604
2605
2606
2607
2608
2609
2610
2611
2612
2613
2614
2615
2616
2617
2618
2619
2620
2621
2622